

# Three-dimensional simulations of stellar core collapse in full general relativity: Nonaxisymmetric dynamical instabilities

Masaru Shibata and Yu-ichirou Sekiguchi

*Graduate School of Arts and Sciences, University of Tokyo, Tokyo, 153-8902, Japan*

We perform fully general relativistic simulations of rotating stellar core collapse in three spatial dimension. The hydrodynamic equations are solved using a high-resolution shock-capturing scheme. A parametric equation of state is adopted to model collapsing stellar cores and neutron stars following Dimmelmeier et al. The early stage of the collapse is followed by an axisymmetric code. When the stellar core becomes compact enough, we start a three-dimensional simulation adding a bar-mode nonaxisymmetric density perturbation. The axisymmetric simulations are performed for a wide variety of initial conditions changing the rotational velocity profile, parameters of the equations of state, and the total mass. It is clarified that the maximum density, the maximum value of the compactness, and the maximum value of the ratio of the kinetic energy  $T$  to the gravitational potential energy  $W$  ( $\beta \equiv T/W$ ) achieved during the stellar collapse and bounce depend sensitively on the velocity profile and the total mass of the initial core, and equations of state. It is also found that for all the models with high degree of differential rotation, a funnel structure is formed around the rotational axis after the formation of neutron stars. For selected models in which the maximum value of  $\beta$  is larger than  $\sim 0.27$ , three-dimensional numerical simulations are performed. It is found that the bar-mode dynamical instability sets in for the case that the following conditions are satisfied: (i) the progenitor of the stellar core collapse should be rapidly rotating with the initial value of  $0.01 \lesssim \beta \lesssim 0.02$ , (ii) the degree of differential rotation for the velocity profile of the initial condition should be sufficiently high, and (iii) a depletion factor of pressure in an early stage of collapse should be large enough to induce a significant contraction to form a compact stellar core for which an efficient spin-up can be achieved surmounting the strong centrifugal force. As a result of the onset of the bar-mode dynamical instabilities, the amplitude of gravitational waves can be by a factor of  $\sim 10$  larger than that in the axisymmetric collapse. It is found that a dynamical instability with the  $m = 1$  mode is also induced for the dynamically unstable cases against the bar-mode, but the perturbation does not grow significantly and, hence, it does not contribute to an outstanding amplification of gravitational waves. No evidence for fragmentation of the protoneutron stars is found in the first a few 10 msec after the bounce.

04.25.Dm, 04.30.-w, 04.40.Dg

## I. INTRODUCTION

One of the most important issues of hydrodynamic simulations in general relativity is to clarify stellar core collapse to a neutron star or a black hole. The formation of neutron stars and black holes is among the most promising sources of gravitational waves. This fact has stimulated numerical simulations for the stellar core collapse [1–12]. However, most of these works have been done in the Newtonian framework and in the assumption of axial symmetry. As demonstrated in [10,12], general relativistic effects modify the dynamics of the collapse and the gravitational waveforms significantly in the formation of neutron stars. Thus, the simulation should be performed in the framework of general relativity. The assumption of axial symmetry is appropriate for the case that the rotating stellar core is not rapidly rotating. However, for the sufficiently rapidly rotating cases, nonaxisymmetric instabilities may grow during the collapse and the bounce [7]. As a result, the amplitude of gravitational waves may be increased significantly.

To date, there has been no general relativistic work for the stellar core collapse in *three spatial dimensions*. Three-dimensional simulations of the stellar core collapse have been performed only in the framework of Newtonian gravity [4,7]. Hydrodynamic simulations for gravitational collapse or for the onset of nonaxisymmetric instabilities of rotating *neutron stars* in full general relativity have been performed so far [13–17], but no simulation has been done for the rotating stellar core collapse to a neutron star or a black hole. In this paper, we present the first numerical results of three-dimensional simulations for rapidly rotating stellar core collapse in full general relativity.

Three-dimensional simulation is motivated by two major purposes. One is to clarify the criterion for the onset of nonaxisymmetric dynamical instabilities during the collapse, and the outcome after the onset of the instabilities. So far, a number of numerical simulations have illustrated that rapidly rotating stars *in isolation and in equilibrium* are often subject to nonaxisymmetric dynamical instabilities not only in Newtonian theory [18–28], but also in post-Newtonian approximation [29], and in general relativity [15]. These simulations have shown that the dynamical

bar-mode instabilities set in (i) when the ratio of the kinetic energy  $T$  to the gravitational potential energy  $W$  (hereafter  $\beta \equiv T/W$ ) is larger than  $\sim 0.27$  or (ii) when the rotating star is highly differentially rotating, even for  $\beta \ll 0.27$  [28]. As a result of the onset of the nonaxisymmetric instabilities, a bar and spiral arms are formed which can redistribute angular momentum profile and change the density profile of the star. Also, a burst-type and subsequent quasiperiodic gravitational waves with a high amplitude can be emitted in the case of rapidly rotating neutron stars [22,28,15]. However, the numerical simulations have been performed mostly for isolated rotating stars in equilibrium. To our knowledge, [7] is only one published paper in which the nonaxisymmetric dynamical instabilities *during stellar core collapse* have been investigated. In [7], the authors performed Newtonian simulations for a few models and indicated that the dynamical instability sets in only for the case that the value of  $\beta$  exceeds much beyond 0.27. Such condition is satisfied only when the progenitor of the collapse is rapidly and highly differentially rotating and the depletion of the internal energy in an early stage of the collapse is large enough to produce a very compact core for which a significant spin-up can be achieved surmounting the strong centrifugal force [6].

Although the previous Newtonian work [7] indicated a criterion for the onset of nonaxisymmetric dynamical instabilities, many unclear points still remain unsolved as follows. First, in the Newtonian analysis [7], the authors adopted a parametric equation of state, and performed simulations changing its own parameters. They found that for the onset of the nonaxisymmetric instability during collapse, a soft equation of state with  $\Gamma_1 = 1.28$  and  $\Gamma_2 = 2.5$  is necessary (see Sec. II B for the definition of  $\Gamma_1$  and  $\Gamma_2$ ). Unfortunately, in the equations of state that they adopted, the maximum gravitational mass for cold spherical neutron stars in general relativity becomes  $\approx 1.3M_\odot$  (see Table I), which is too small to be adopted as a plausible equation of state in general relativistic simulations since the maximum mass of neutron stars for a given equation of state should be larger than  $\approx 1.44M_\odot$  which is the precisely determined mass of a neutron star in PSRB1913+16 [30]. A study with more plausible equations of state is required.

Second, the authors in [7] focus little on the instabilities associated with  $m = 2$  bar mode, although it is the fastest growing mode of the nonaxisymmetric dynamical instabilities for equilibrium stars in most cases. (Here,  $m$  denotes the azimuthal quantum number.) Thus, the criterion for the onset of the bar-mode instabilities are not still clear. Also, they paid little attention to the bar-mode dynamical instabilities for highly differentially rotating cases such as those recently reported in [28]. This instability can set in even for a small value of  $\beta < 0.27$ . This implies that for highly differentially rotating initial conditions, attention should be also paid for small values of  $\beta$ .

Third, in general relativity, the collapsed core can reach a more compact state than that simulated in the Newtonian theory due to the fact that self-gravity becomes stronger [10]. As a result, more efficient spin-up will be achieved. Therefore, the probability for the onset of nonaxisymmetric dynamical instabilities would be underestimated in the Newtonian simulation. This suggests that general relativistic analysis may be crucial for the study of nonaxisymmetric dynamical instabilities.

Finally, in [7], the mass of the stellar core adopted is set to be in a narrow range between  $1.5$  and  $1.7M_\odot$ . According to the theory of stellar evolutions, in a very massive star of low metallicity with the initial mass  $50M_\odot \lesssim M \lesssim 100M_\odot$ , the produced iron core may become  $2\text{--}3M_\odot$  [31–33]. This indicates that the mass of the core in nature may be in a wide range between  $\sim 1M_\odot$  and  $\sim 3M_\odot$ . With the increase of the mass, the self-gravity becomes stronger, and hence, the collapsed stellar core can reach a more compact state for which a spin-up may be enhanced effectively. Thus, the larger core mass may increase the probability for the onset of nonaxisymmetric dynamical instabilities.

Motivated by the questions mentioned above, we perform general relativistic simulations choosing rapidly and highly differentially rotating massive stars with plausible equations of state and with a wide mass range. Following [7], we adopt a parametric equation of state. However, we choose sets of the parameters in which the maximum Arnowitt-Deser-Misner (ADM) mass of cold spherical neutron star becomes  $\approx 1.6M_\odot$ . With this setting, we choose the mass of the stellar core in the range between  $\sim 1.5$  and  $\sim 3M_\odot$ . Furthermore, we pay particular attention to the bar-mode instabilities which are likely to be the fastest growing mode.

Another major role of three-dimensional simulations for the stellar core collapse is to determine the amplitude and the characteristic frequency of gravitational waves in the case that the nonaxisymmetric dynamical instabilities set in. Axisymmetric numerical simulations have clarified that the amplitude of gravitational waves emitted in the stellar core collapse is at most several  $\times 10^{-23}$  at a distance of 10 Mpc (e.g., [10]), and the frequency is between 100 Hz and 1 kHz. Although the frequency is in the most sensitive band of the laser interferometric gravitational wave detectors [34], the value of the amplitude is too small to be detected if the stellar core collapse occurs outside our local group of galaxies. In the three-dimensional process, on the other hand, the amplitude is often by a factor of  $\sim 10$  larger than that in the axisymmetric phenomena because of the increase of the degree of asymmetry. Hence, if the nonaxisymmetric instabilities set in, the stellar core collapse may become a much stronger emitter of gravitational waves than that considered so far.

This paper is organized as follows. In Sec. II, we briefly review our formulation of general relativistic simulation, equations of state adopted in this paper, and methods for extraction of gravitational waves. In Sec. III, initial conditions and computational setting are described. In Sec. IV, numerical results of axisymmetric simulations are presented paying attention to the value of  $\beta$  and to the profiles of the density and the angular velocity of the outcomes.

In Sec. V, numerical results of three-dimensional simulations are presented, clarifying the criterion for the onset of bar-mode dynamical instabilities. Gravitational waveforms emitted in the growth of the bar-mode dynamical instabilities are also presented. Sec. VI is devoted to a summary. Throughout this paper, we adopt the geometrical units in which  $G = c = 1$  where  $G$  and  $c$  are the gravitational constant and speed of light, respectively.

## II. FORMULATION

### A. Summary of basic equations and implementations

We perform hydrodynamic simulations in full general relativity using the same formulation as in [35,36], to which the reader may refer for details and basic equations. The fundamental variables for the hydrodynamics are  $\rho$ : rest mass density,  $\varepsilon$ : specific internal energy,  $P$ : pressure,  $u^\mu$ : four velocity, and

$$v^i = \frac{dx^i}{dt} = \frac{u^i}{u^t}, \quad (1)$$

where subscripts  $i, j, k, \dots$  denote  $x, y$  and  $z$ , and  $\mu$  the spacetime components. As the fundamental variables to be evolved in the numerical simulations, we define a weighted density  $\rho_*$ , a weighted four-velocity  $\hat{u}_i$ , and a specific energy density  $\hat{e}$  as

$$\rho_* = \rho w e^{6\phi}, \quad (2)$$

$$\hat{u}_i \equiv h u_i, \quad (3)$$

$$\hat{e} \equiv h w - \frac{P}{\rho w}, \quad (4)$$

where  $e^\phi$  denotes the conformal factor,  $w \equiv \alpha u^t$ , and  $h \equiv 1 + \varepsilon + P/\rho$ . Here,  $\hat{e}$  is computed from  $T_{\mu\nu} n^\mu n^\nu / (\rho w)$  where  $T_{\mu\nu}$  and  $n^\mu$  denote the energy-momentum tensor and a timelike unit normal vector. General relativistic hydrodynamic equations are solved using a high-resolution shock-capturing scheme [37,35]. In axisymmetric and three-dimensional simulations, the cylindrical and Cartesian coordinates are used, respectively. The details of our hydrodynamic code are described in [35].

For the following, we define the total baryon rest-mass, internal energy, and rotational kinetic energy of the system as

$$M_* = \int d^3x \rho_*, \quad (5)$$

$$U = \int d^3x \rho_* \varepsilon, \quad (6)$$

$$T = \frac{1}{2} \int d^3x \rho_* \hat{u}_\varphi v^\varphi, \quad (7)$$

where  $M_*$  is the conserved quantity. The definitions of  $U$  and  $T$  agree with those for axisymmetric rotating stars in equilibrium [39]. In the axisymmetric case, the angular momentum  $J$  is a conserved quantity, and defined by

$$J = \int d^3x \rho_* \hat{u}_\varphi. \quad (8)$$

Note that in the nonaxisymmetric case, the equation of  $J$  has a different form (e.g., [13]).

The fundamental variables for the geometry are  $\alpha$ : lapse function,  $\beta^k$ : shift vector,  $\gamma_{ij}$ : three-metric,  $\gamma = e^{12\phi} = \det(\gamma_{ij})$ : trace of the three-metric,  $\tilde{\gamma}_{ij} = e^{-4\phi} \gamma_{ij}$ : conformal three-metric, and  $K_{ij}$ : extrinsic curvature. We evolve  $\tilde{\gamma}_{ij}$ ,  $\phi$ ,  $\tilde{A}_{ij} \equiv e^{-4\phi} (K_{ij} - \gamma_{ij} K_k^k)$ , and the trace of the extrinsic curvature  $K_k^k$  together with the three auxiliary variables  $F_i \equiv \delta^{jk} \partial_j \tilde{\gamma}_{ik}$  with an unconstrained free evolution code as in [40,13,41,35]. The Einstein equations are solved in the Cartesian coordinates. In the axisymmetric case, the Cartoon method is used [42,43]. In both cases, the equatorial reflection symmetry is assumed. The outer boundary conditions we adopt are the same as in the previous papers (e.g., [13,41,35]).

As the slicing condition, we impose an ‘‘approximate’’ maximal slice condition ( $K_k^k \approx 0$ ) which is the same as that adopted in previous papers (e.g., [13,15,41]). As the spatial gauge condition, we adopt a hyperbolic gauge condition [47,36] in which we solve

$$\partial_t \beta^k = \tilde{\gamma}^{kl} (F_l + \Delta t \partial_t F_l), \quad (9)$$

where  $\Delta t$  denotes a time step in numerical computation.

During numerical simulations, violations of the Hamiltonian constraint and conservation of mass and angular momentum are monitored as code checks. Numerical results for several test calculations, including stability and collapse of nonrotating and rotating neutron stars, have been described in [35]. The axisymmetric code has been used for simulations of stellar core collapse to neutron stars and black holes, producing numerically convergent results [12]. The three-dimensional code has been used particularly for simulations of merger of binary neutron stars [41,36]. In [36], the details of the latest implementation are described, and we illustrate that accurate and convergent numerical results on the outcomes after the merger as well as on gravitational waveforms can be obtained with the present code.

## B. Equations of state

A parametric equation of state is adopted following Müller and his collaborators [6,10]. In this equation of state, one assumes that the pressure consists of the sum of polytropic and thermal parts as

$$P = P_P + P_{\text{th}}. \quad (10)$$

The polytropic part is given by  $P_P = K_P(\rho)\rho^{\Gamma(\rho)}$  where  $K_P$  and  $\Gamma$  are not constants but functions of  $\rho$ . This part corresponds to the cold (zero-temperature) part of the equation of state. In this paper, we follow [10] for the choice of  $K_P(\rho)$  and  $\Gamma(\rho)$ : For the density smaller than the nuclear density which is defined as  $\rho_{\text{nuc}} \equiv 2 \times 10^{14} \text{ g/cm}^3$ ,  $\Gamma = \Gamma_1 (= \text{const})$  is set to be  $\lesssim 4/3$ , and for  $\rho \geq \rho_{\text{nuc}}$ ,  $\Gamma = \Gamma_2 (= \text{const}) \geq 2$ . Thus,

$$P_P = \begin{cases} K_1 \rho^{\Gamma_1}, & \rho \leq \rho_{\text{nuc}}, \\ K_2 \rho^{\Gamma_2}, & \rho \geq \rho_{\text{nuc}}, \end{cases} \quad (11)$$

where  $K_1$  and  $K_2$  are constants. Since  $P_P$  should be continuous, the relation,  $K_2 = K_1 \rho_{\text{nuc}}^{\Gamma_1 - \Gamma_2}$ , is required. Following [6,10], the value of  $K_1$  is fixed to be  $5 \times 10^{14}$  in the cgs unit. With this choice, a realistic equation of state for  $\rho < \rho_{\text{nuc}}$ , in which the degenerate pressure of electrons is dominant, is approximated. Since the specific internal energy should be continuous at  $\rho = \rho_{\text{nuc}}$ , the polytropic specific internal energy  $\varepsilon_P$  is defined as

$$\varepsilon_P = \begin{cases} \frac{K_1}{\Gamma_1 - 1} \rho^{\Gamma_1 - 1}, & \rho \leq \rho_{\text{nuc}}, \\ \frac{K_2}{\Gamma_2 - 1} \rho^{\Gamma_2 - 1} + \frac{(\Gamma_2 - \Gamma_1) K_1 \rho_{\text{nuc}}^{\Gamma_1 - 1}}{(\Gamma_1 - 1)(\Gamma_2 - 1)}, & \rho \geq \rho_{\text{nuc}}. \end{cases} \quad (12)$$

With this setting, a realistic equation of state for cold nuclear matter is mimicked for an appropriate choice of  $\Gamma_1$  and  $\Gamma_2$ .

An advantage of the parametric equations of state is that we can investigate the dependence of the dynamics of stellar collapse on the equations of state systematically and very easily by changing the values of  $\Gamma_1$  and  $\Gamma_2$  appropriately. A more realistic simulation with a realistic equation of state should be performed at the goal in this research field. However, the equations of state for  $\rho > \rho_{\text{nuc}}$  are not still well-known. Also, because of complexity of the microphysical processes, in simulations with such realistic equations of state, it is often not easy to extract essential physical properties of stellar core collapse such as key quantities that determine the maximum density in the collapse, the collapse time scale, the maximum value of  $T/W$ , the profiles of the density and angular velocity of formed protoneutron stars,  $T/W$  of formed protoneutron stars, nonaxisymmetric dynamical stabilities, and amplitude of gravitational waves. Simulations with the parametric equations of state are helpful to systematically answer these questions.

In this paper, we choose  $(\Gamma_1, \Gamma_2) = (1.3, 2.5)$ ,  $(1.32, 2.25)$ , and  $(1.28, 2.75)$ . In Table I, we list the maximum mass and the corresponding density at the center for the three sets of  $\Gamma_1$  and  $\Gamma_2$  with  $\rho_{\text{nuc}} = 2 \times 10^{14} \text{ g/cm}^3$ . In all three cases, the maximum ADM mass becomes about  $1.6M_\odot$  which is a reasonable value for neutron stars [48]. As a default, we set  $\Gamma_1 = 1.3$  and  $\Gamma_2 = 2.5$  in the following. In a previous Newtonian three-dimensional simulation [7], a different set as  $\Gamma_1 = 1.28$  and  $\Gamma_2 = 2.5$  is chosen, and the authors have found that only for such small value of  $\Gamma_1$ , nonaxisymmetric dynamical instabilities are induced. The choice of this set is acceptable in the Newtonian framework, but in general relativity it should not be adopted because with this choice, the maximum mass of a cold spherical neutron star becomes about  $1.3M_\odot$ , which is too small for the maximum mass. Such choice should be excluded in general relativistic simulations.

$\Gamma_1$	$\Gamma_2$	$M_*(M_\odot)$	$M(M_\odot)$	$\rho_c(\text{g/cm}^3)$
1.3	2.5	1.810	1.600	2.87e15
1.32	2.25	1.754	1.623	2.39e15
1.28	2.75	1.869	1.597	3.18e15
1.28	2.5	1.486	1.298	4.42e15

TABLE I. Maximum baryon rest-mass, ADM mass, and the corresponding central density for spherical neutron stars of cold, parametric equations of state (11) for several choices of  $\Gamma_1$  and  $\Gamma_2$ . The first three sets of  $\Gamma_1$  and  $\Gamma_2$  are adopted in the paper. The fourth set of the equation of state which is used in Refs. [6,7] is too soft and the maximum ADM mass for cold, spherical neutron stars is too small to be adopted as a realistic parameter set.

The thermal part of the pressure  $P_{\text{th}}$  plays an important role in the case that shocks are generated.  $P_{\text{th}}$  is related to the thermal energy density  $\varepsilon_{\text{th}} \equiv \varepsilon - \varepsilon_{\text{P}}$  as

$$P_{\text{th}} = (\Gamma_{\text{th}} - 1)\rho\varepsilon_{\text{th}}. \quad (13)$$

For simplicity, the value of  $\Gamma_{\text{th}}$ , which determines the strength of shocks, is chosen to be equal to  $\Gamma_1 (\approx 1.3)$ . Our previous numerical work [12] showed that the results depend very weakly on the value of  $\Gamma_{\text{th}}$  as far as it is in the range between  $\sim 1.3$  and  $5/3$ .

For the simulation, first, equilibrium rotating stars with  $\Gamma = 4/3$  polytrope are given. Then, the simulations are started with equations of state (10). Since the value of the adiabatic index is slightly decreased from  $\Gamma = 4/3$  to  $\Gamma_1 (< 4/3)$ , the collapse is triggered. The equilibrium states are computed adopting the polytropic equation of state

$$P = K_0\rho^{4/3}, \quad (14)$$

where  $K_0$  is the adiabatic constant. In this paper,  $K_0$  is set to be  $5 \times 10^{14}$ ,  $7 \times 10^{14}$ , and  $8 \times 10^{14} \text{ cm}^3/\text{s}^2/\text{g}^{1/3}$ . The latter two are adopted to increase the mass of the progenitor of stellar collapse: For the  $\Gamma = 4/3$  polytrope, the mass (both the baryon rest-mass and the ADM mass) of the stars is approximately written as  $4.555(K_0/G)^{3/2} \text{ g}$ , which depends very weakly on the rotational velocity profile [48] (cf. Table II). This implies that for  $K_{14} \equiv K_0/10^{14} \text{ cm}^3/\text{s}^2/\text{g}^{1/3} = 5, 7, \text{ and } 8$ , the mass is about 1.5, 2.5, and  $3M_\odot$ , respectively. Thus, for  $K_{14} \geq 7$ , the total mass of the system is much larger than the maximum allowed mass of the cold spherical neutron stars chosen in this paper  $\approx 1.6M_\odot$ .

For  $K_0 = K_{\text{deg}} \approx 5 \times 10^{14} \text{ cm}^3/\text{s}^2/\text{g}^{1/3}$  which is chosen in previous papers [6,10,12], a soft equation of state governed only by the electron degenerate pressure is approximated well [48,49]. On the other hand, the radiation pressure is also approximated by the  $\Gamma = 4/3$  polytropic equation of state. Thus, by choosing  $K_0 > K_{\text{deg}}$ , we may consider that the pressure is composed of the sum of the electron degenerate pressure and the radiation pressure with the ratio  $K_{\text{deg}}$  to  $K_{\text{rad}} \equiv K_0 - K_{\text{deg}}$  as

$$P = K_{\text{deg}}\rho^{4/3} + K_{\text{rad}}\rho^{4/3}. \quad (15)$$

In the simulation,  $K_1$  is related to  $K_{\text{deg}}$  by  $K_1 = K_{\text{deg}}\rho_0^{4/3-\Gamma_1}$  where we set  $\rho_0 = 1 \text{ g/cm}^3$ . The specific internal energy is given by

$$\varepsilon = 3K_0\rho^{1/3}, \quad (16)$$

and the pressure at the initial stage is written as

$$P = 3(\Gamma_1 - 1)K_0\rho^{4/3}, \quad (17)$$

implying that for  $\Gamma_1 < 4/3$ , the pressure is depleted by  $(4 - 3\Gamma_1) = 4 - 16\%$  for  $\Gamma_1 = 1.32 - 1.28$  at the initial stage. Namely, in this setting, with the smaller value of  $\Gamma_1$ , the pressure for a given value of  $\rho < \rho_{\text{nuc}}$  becomes smaller, and also, the deletion factors of the pressure and the internal energy at the initial condition are larger. As shown in Secs. IV and V, the effect associated with the small change in  $\Gamma_1$  significantly modifies the dynamics of the collapse and the stability against nonaxisymmetric dynamical deformation.

### C. Wave extraction methods

We extract gravitational waves using two methods. One is a gauge-invariant wave extraction method in which we perturbatively compute the Moncrief variables in a flat spacetime background [46] as we have used in our series of

papers (e.g., [45]). To compute them, first, we split  $\gamma_{ij}$  into  $\eta_{ij} + \sum_{lm} \zeta_{ij}^{lm}$  in the spherical polar coordinates, where  $\eta_{ij}$  is the flat metric and  $\zeta_{ij}^{lm}$  is given by

$$\zeta_{ij}^{lm} = \begin{pmatrix} H_{2lm}Y_{lm} & h_{1lm}\partial_\theta Y_{lm} & h_{1lm}\partial_\varphi Y_{lm} \\ * & r^2(K_{lm}Y_{lm} + G_{lm}W_{lm}) & r^2G_{lm}X_{lm} \\ * & * & r^2\sin^2\theta(K_{lm}Y_{lm} - G_{lm}W_{lm}) \end{pmatrix} + \begin{pmatrix} 0 & -C_{lm}\partial_\varphi Y_{lm}/\sin\theta & C_{lm}\partial_\theta Y_{lm}\sin\theta \\ * & r^2D_{lm}X_{lm}/\sin\theta & -r^2D_{lm}W_{lm}\sin\theta \\ * & * & -r^2D_{lm}X_{lm}\sin\theta \end{pmatrix}. \quad (18)$$

Here, \* denotes the symmetric components. The quantities  $H_{2lm}$ ,  $h_{1lm}$ ,  $K_{lm}$ ,  $G_{lm}$ ,  $C_{lm}$ , and  $D_{lm}$  are functions of  $r$  and  $t$ , and are calculated by performing integrals over a two-sphere of a given coordinate radius [see [40] for details].  $Y_{lm}$  is the spherical harmonic function, and  $W_{lm}$  and  $X_{lm}$  are

$$W_{lm} \equiv \left[ (\partial_\theta)^2 - \cot\theta\partial_\theta - \frac{1}{\sin^2\theta}(\partial_\varphi)^2 \right] Y_{lm}, \quad X_{lm} \equiv 2\partial_\varphi \left[ \partial_\theta - \cot\theta \right] Y_{lm}. \quad (19)$$

The gauge-invariant variables of even and odd parities are defined by

$$R_{lm}^E(t, r) \equiv \sqrt{\frac{2(l-2)!}{(l+2)!}} \left\{ 4k_{2lm} + l(l+1)k_{1lm} \right\}, \quad (20)$$

$$R_{lm}^O(t, r) \equiv \sqrt{\frac{2(l+2)!}{(l-2)!}} \left( \frac{C_{lm}}{r} + r\partial_r D_{lm} \right), \quad (21)$$

where

$$k_{1lm} \equiv K_{lm} + l(l+1)G_{lm} + 2r\partial_r G_{lm} - 2\frac{h_{1lm}}{r}, \quad (22)$$

$$k_{2lm} \equiv \frac{H_{2lm}}{2} - \frac{1}{2}\frac{\partial}{\partial r} \left[ r \{ K_{lm} + l(l+1)G_{lm} \} \right]. \quad (23)$$

Using the gauge-invariant variables, the energy luminosity and the angular momentum flux of gravitational waves can be defined by

$$\frac{dE}{dt} = \frac{r^2}{32\pi} \sum_{l,m} \left[ |\partial_t R_{lm}^E|^2 + |\partial_t R_{lm}^O|^2 \right], \quad (24)$$

$$\frac{dJ}{dt} = \frac{r^2}{32\pi} \sum_{l,m} \left[ |m(\partial_t R_{lm}^E)R_{lm}^E| + |m(\partial_t R_{lm}^O)R_{lm}^O| \right]. \quad (25)$$

The total radiated energy and angular momentum are calculated by

$$\Delta E(t) = \int_0^t dt \frac{dE}{dt}, \quad \Delta J(t) = \int_0^t dt \frac{dJ}{dt}. \quad (26)$$

In this paper, we pay attention only to even-parity modes with  $l = 2$  which are the dominant modes.

To search for the characteristic frequencies of gravitational waves, the Fourier spectra are computed by

$$\bar{R}_{lm}^I(f) = \int_{t_i}^{t_f} e^{2\pi i f t} R_{lm}^I dt, \quad (27)$$

where  $I$  denotes E and O. In the analysis,  $t_f$  is chosen as the time at which the simulation is stopped. Before  $t < r_{\text{obs}}$  where  $r_{\text{obs}}$  denotes a radius at which gravitational waves are extracted, no waves propagate to  $r_{\text{obs}}$ , so that we choose  $t_i \approx r_{\text{obs}}$ .

Using the Fourier spectrum, the energy power spectrum is written as

$$\frac{dE}{df} = \frac{\pi}{4} r^2 \sum_{l \geq 2, m \geq 0} f^2 (|\bar{R}_{lm}^E(f)|^2 + |\bar{R}_{lm}^O(f)|^2) \quad (f > 0), \quad (28)$$

where for  $m \neq 0$ , we define

$$\bar{R}_{lm}^I \equiv \sqrt{|\bar{R}_{lm}^I(f)|^2 + |\bar{R}_{l-m}^I(f)|^2} \quad (m > 0). \quad (29)$$

Note that in deriving Eq. (28), we use the relation  $|\bar{R}_{lm}^I(-f)| = |\bar{R}_{lm}^I(f)|$ .

Computation of gravitational waves is also carried out in terms of a quadrupole formula which is described in [44,12]. As shown in [44], a kind of quadrupole formula can provide an approximate gravitational waveform from oscillating compact stars. The quadrupole formula is in particular useful when the amplitude of gravitational waves is smaller than the numerical noise because in such case, it is difficult to extract gravitational waves from the metric in the wave zone.

In quadrupole formulas, we compute gravitational waves from

$$h_{ij} = \left[ P_i^k P_j^l - \frac{1}{2} P_{ij} P^{kl} \right] \left( \frac{2}{r} \frac{d^2 I_{kl}}{dt^2} \right), \quad (30)$$

where  $I_{ij}$  and  $P_i^j = \delta_{ij} - n_i n_j$  ( $n_i = x^i/r$ ) denote a tracefree quadrupole moment and a projection tensor.

In fully general relativistic and dynamical spacetimes, there is no unique definition for the quadrupole moment  $I_{ij}$ . Following [44,12], we choose the formula as

$$I_{ij} = \int \rho_* x^i x^j d^3x. \quad (31)$$

Then, using the continuity equation, we can compute the first time derivative as

$$\dot{I}_{ij} = \int \rho_* (v^i x^j + x^i v^j) d^3x. \quad (32)$$

To compute  $\ddot{I}_{ij}$ , we carried out the finite differencing of the numerical result for  $\dot{I}_{ij}$ .

In this paper, we focus only on  $l = 2$  mass quadrupole modes. Then, the gravitational waveforms are described by

$$h_+ = \frac{1}{r} \left[ \frac{\ddot{I}_{xx} - \ddot{I}_{yy}}{2} (1 + \cos^2 \theta) \cos(2\varphi) + \ddot{I}_{xy} (1 + \cos^2 \theta) \sin(2\varphi) + \left( \ddot{I}_{zz} - \frac{\ddot{I}_{xx} + \ddot{I}_{yy}}{2} \right) \sin^2 \theta \right], \quad (33)$$

$$h_\times = \frac{2}{r} \left[ -\frac{\ddot{I}_{xx} - \ddot{I}_{yy}}{2} \cos \theta \sin(2\varphi) + \ddot{I}_{xy} \cos \theta \cos(2\varphi) \right], \quad (34)$$

in the quadrupole formula, and

$$h_+ = \frac{1}{r} \left[ \sqrt{\frac{5}{64\pi}} \{ R_{22+} (1 + \cos^2 \theta) \cos(2\varphi) + R_{22-} (1 + \cos^2 \theta) \sin(2\varphi) \} + \sqrt{\frac{15}{64\pi}} R_{20} \sin^2 \theta \right], \quad (35)$$

$$h_\times = \frac{2}{r} \sqrt{\frac{5}{64\pi}} \left[ -R_{22+} \cos \theta \sin(2\varphi) + R_{22-} \cos \theta \cos(2\varphi) \right], \quad (36)$$

in the gauge-invariant wave extraction where

$$R_{22\pm} = \frac{R_{22}^E \pm R_{2-2}^E}{\sqrt{2}} r, \quad (37)$$

$$R_{20} = R_{20}^E r. \quad (38)$$

For derivation of  $h_+$  and  $h_\times$ , we assume that the wave part of the spatial metric in the wave zone is written as

$$dl^2 = dr^2 + r^2 [(1 + h_+) d\theta^2 + \sin^2 \theta (1 - h_+) d\varphi^2 + 2 \sin \theta h_\times d\theta d\varphi], \quad (39)$$

and set  $I_{xz} = I_{yz} = 0$  and  $R_{2\pm 1}^E = 0$  since we assume the reflection symmetry with respect to the equatorial plane.

In the following, we present

$$A_+ = \ddot{I}_{xx} - \ddot{I}_{yy}, \quad (40)$$

$$A_\times = 2\ddot{I}_{xy}, \quad (41)$$

$$A_0 = \frac{2\ddot{I}_{zz} - \ddot{I}_{xx} - \ddot{I}_{yy}}{2}, \quad (42)$$

in the quadrupole formula, and as the corresponding variables,

$$R_+ = \sqrt{\frac{5}{16\pi}} R_{22+}, \quad (43)$$

$$R_\times = \sqrt{\frac{5}{16\pi}} R_{22-}, \quad (44)$$

$$R_0 = \sqrt{\frac{15}{64\pi}} R_{20}, \quad (45)$$

in the gauge-invariant wave extraction method. These provide the amplitude of a given mode measured by an observer located in the most optimistic direction.

### III. SETTING

#### A. Initial conditions for axisymmetric simulation

Rotating stellar cores in equilibrium with the  $\Gamma = 4/3$  polytropic equation of state [Eq. (14)] are prepared for the initial conditions. Following [10,12], the maximum density is chosen as  $\rho_{\max} = 10^{10} \text{ g/cm}^3$  irrespective of the velocity profile and the value of  $K_0$ .

The velocity profiles of equilibrium rotating stellar cores are given according to a popular relation [50,51,10]

$$u^t u_\varphi = \varpi_d^2 (\Omega_a - \Omega), \quad (46)$$

where  $\Omega = v^\varphi$  denotes the angular velocity,  $\Omega_a$  is that along the rotational axis, and  $\varpi_d$  is a constant. In the Newtonian limit, the rotational profile is written as

$$\Omega = \Omega_a \frac{\varpi_d^2}{\varpi^2 + \varpi_d^2}. \quad (47)$$

Thus,  $\varpi_d$  indicates the steepness of differential rotation. Since the compactness of the initial data adopted in this paper is not so large with  $M/R \sim 10^{-3}$ , where  $R$  denotes a stellar radius, that general relativistic effects are weak. As a result, the profile of the rotational angular velocity is approximately written by Eq. (47). In the following, we adopt rigidly rotating models in which  $\varpi_d \rightarrow \infty$ , and differentially rotating models with  $A \equiv \varpi_d/R_e = 0.25$  and  $0.1$ , where  $R_e$  is the coordinate radius at the equatorial surface. The ratio of the angular velocity at the equatorial surface to  $\Omega_a$  is  $\approx 1/17$  and  $1/101$  for  $A = 0.25$  and  $0.1$ , indicating that Eq. (47) is approximately satisfied. We pay particular attention to the case with high degrees of differential rotation in this paper, since in the collapse, a large value of  $\beta$  can be achieved only for such cases. Indeed, a study for presupernova evolution of rotating massive stars [38] indicates that the velocity profile of the iron core just before the onset of collapse may be differentially rotating.

As introduced in Sec. I, the ratio ( $\beta = T/W$ ) of the rotational kinetic energy  $T$  to the gravitational potential energy  $W$  is often referred in the following. In general relativity,  $W$  is defined by [39]

$$W = M_* + U + T - M. \quad (48)$$

Here,  $W$  is defined to be positive. For stable rotating stars in equilibrium with  $\Gamma = 4/3$ ,  $M_*$  is nearly equal to  $M$ . Thus,

$$W \approx U + T, \quad \text{and} \quad \beta \approx \frac{T}{U + T}. \quad (49)$$

Even in the dynamical evolution,  $M_*$  is the conserved quantity and  $M$  is approximately conserved in the case that luminosity of gravitational waves is small. Thus, if other components of the energy such as the kinetic energy associated with radial velocity are small, the above approximate relation for  $\beta$  in terms of  $U$  and  $T$  may be used even in the dynamical spacetime [see also discussion around Eq. (55)].

In Table II, several quantities for the models adopted in the present numerical computation are summarized. In the first column, we describe the name of each model. We refer to the models with  $(K_{14}, A) = (5, \infty), (5, 0.1), (7, \infty), (7, 0.25), (7, 0.1), (8, \infty),$  and  $(8, 0.1)$  as M5a, M5c, M7a, M7b, M7c, M8a, and M8c, respectively.

For the rigidly rotating case with  $A \rightarrow \infty$ , the magnitude of the angular velocity has to be smaller than the Kepler angular velocity at the equatorial surface. This restricts the maximum value of  $\beta$  to be smaller than  $\approx 0.0089$  for

Model	$A$	$K_0$	$M_*$	$\beta_{\text{init}}$	$J/M^2$	$P_0$	$R_e$	$\alpha_{\text{Min}}$	$\rho_{\text{Max}}$	$\beta_{\text{max}}$	Outcome
M5a1	$\infty$	5e14	1.503	0.00891	1.235	1.53	2.27e3	0.76	6.6e14	0.11	NS
M5c1	0.1	5e14	1.545	0.0177	1.201	0.127	1.48e3	0.79	3.2e14	0.28	O-A
M5c2	0.1	5e14	1.521	0.0124	1.028	0.155	1.50e3	0.74	5.0e14	0.28	O-A $\rightarrow$ NS
M5c3	0.1	5e14	1.496	0.00730	0.784	0.212	1.53e3	0.71	6.6e14	0.21	NS
M7a1	$\infty$	7e14	2.476	0.00886	1.045	1.53	2.68e3	0.57	1.1e15	0.10	NS
M7a2	$\infty$	7e14	2.458	0.00649	0.888	1.77	2.16e3	0.56	1.1e15	0.081	NS
M7a3	$\infty$	7e14	2.449	0.00526	0.792	1.97	2.06e3	—	—	—	BH
M7a4	$\infty$	7e14	2.438	0.00367	0.663	2.33	1.98e3	—	—	—	BH
M7b1	0.25	7e14	2.579	0.0218	1.423	0.370	1.88e3	0.82	7.9e13	0.26	O-B
M7b2	0.25	7e14	2.545	0.0177	1.283	0.411	1.87e3	0.73	2.6e14	0.29	O-A
M7b3	0.25	7e14	2.514	0.0138	1.134	0.466	1.87e3	0.65	4.8e14	0.29	NS
M7b4	0.25	7e14	2.495	0.0113	1.027	0.515	1.86e3	0.62	6.4e14	0.26	NS
M7b5	0.25	7e14	2.451	0.00543	0.712	0.744	1.85e3	0.55	1.1e15	0.16	NS
M7b6	0.25	7e14	2.434	0.00321	0.547	0.969	1.85e3	0.52	1.4e15	0.10	NS
M7c1	0.1	7e14	2.579	0.0219	1.126	0.111	1.72e3	0.70	3.8e14	0.31	O-A
M7c2	0.1	7e14	2.544	0.0177	1.018	0.127	1.75e3	0.61	6.0e14	0.33	O-A
M7c3	0.1	7e14	2.505	0.0127	0.871	0.155	1.78e3	0.51	9.2e14	0.30	NS
M7c4	0.1	7e14	2.505	0.00994	0.773	0.179	1.79e3	0.46	1.2e15	0.27	NS
M7c5	0.1	7e14	2.464	0.00728	0.664	0.213	1.81e3	0.42	1.4e15	0.22	NS
M7c6	0.1	7e14	2.439	0.00392	0.489	0.296	1.83e3	0.42	1.4e15	0.14	NS
M7c7	0.1	7e14	2.427	0.00232	0.377	0.389	1.83e3	0.44	1.7e15	0.088	NS
M8a1	$\infty$	8e14	3.016	0.00884	0.978	1.54	2.86e3	—	—	—	BH
M8c1	0.1	8e14	3.187	0.0263	1.151	0.0984	1.82e3	0.70	3.0e14	0.31	O-A
M8c2	0.1	8e14	3.141	0.0219	1.055	0.111	1.84e3	0.59	5.4e14	0.34	O-A
M8c3	0.1	8e14	3.099	0.0176	0.953	0.128	1.87e3	0.47	8.4e14	0.35	O-A
M8c4	0.1	8e14	3.052	0.0127	0.815	0.156	1.90e3	0.29	1.5e15	0.30	NS
M8c5	0.1	8e14	3.010	0.00814	0.657	0.200	1.93e3	—	—	—	BH

TABLE II. Quantities for selected set of the initial conditions and the results of collapse are listed.  $K_0$ ,  $M_*$ ,  $P_0$  ( $\equiv 2\pi/\Omega_a$ ),  $R_e$ , and  $\rho_{\text{Max}}$  are shown in units of  $\text{cm}^3/\text{s}^2/\text{g}^{1/3}$ ,  $M_\odot$ , sec, km, and  $\text{g}/\text{cm}^3$ , respectively. Here,  $\rho_{\text{Max}}$  and  $\alpha_{\text{Min}}$  are the maximum and minimum achieved during the whole evolution.  $\beta_{\text{init}}$  and  $\beta_{\text{max}}$  denote the initial value of  $T/W$  and the maximum value of  $T/(T+U)$  achieved during the collapse. The baryon rest-mass  $M_*$  is nearly equal to the ADM mass  $M$  for all the models. In the last column, the outcomes for  $\Gamma_1 = 1.3$ ,  $\Gamma_2 = 2.5$ , and  $\rho_{\text{nuc}} = 2 \times 10^{14} \text{ g}/\text{cm}^3$  are shown. Here, NS, O-A, and O-B denote that the outcomes are neutron star, oscillating star with the maximum density larger than  $\rho_{\text{nuc}}$ , and oscillating star of subnuclear density, respectively. Note that for  $K_0 = 8 \times 10^{14}$  (cgs) and  $A \rightarrow \infty$ , any star collapses to a black hole and that for  $K_0 \leq 6 \times 10^{14}$  (cgs), any star does not collapse to a black hole.

all the values of  $K_0$ . This implies that the angular velocity for models M5a1, M7a1, and M8a1 is approximately maximum among the rigidly rotating cases for a given value of  $K_0$ . The final outcome of M8a1 is a black hole. This implies that any star with  $(K_{14}, A) = (8, \infty)$  collapses to a black hole because the mass is too large and the angular momentum is too small to halt the collapse. On the other hand, for  $K_{14} \leq 6$ , any star does not collapse to a black hole since the mass is not large enough. The detail on the criterion of the formation of black hole is also described in the companion paper [52].

## B. Method of axisymmetric simulation

During the collapse, the maximum density increases from  $10^{10} \text{ g}/\text{cm}^3$  to  $\sim 10^{15} \text{ g}/\text{cm}^3$  in the neutron star formation and to  $\gg 10^{15} \text{ g}/\text{cm}^3$  in the black hole formation. This implies that the characteristic length scale of the system varies by a factor of  $\gtrsim 100$ . In the early phase of the collapse which proceeds in a nearly homologous manner, we may follow the collapse with a relatively small number of grid points by moving the outer boundary inward while decreasing the grid spacing, without increasing the grid number by a large factor. As the collapse proceeds, the central region shrinks more rapidly than the outer region does and, hence, a better grid resolution is necessary to accurately follow such a rapid collapse in the central region. On the other hand, the location of the outer boundaries should not be

changed by a large factor to avoid discarding the matter in the outer envelopes.

To compute such a collapse accurately while saving the CPU time efficiently, a regridding technique as described and used in [53,12] is adopted. The regridding is carried out whenever the characteristic radius of the collapsing star decreases by a factor of a few. At each regridding, the grid spacing is decreased by a factor of 2. All the quantities in the new grid are calculated using the cubic interpolation. To avoid discarding the matter in the outer region, we also increase the grid number at the regridding, keeping a rule that the discarded baryon rest-mass has to be less than 1% of the total.

Specifically,  $N$  and  $L$  in the present work are chosen using a relativistic gravitational potential defined by  $\Phi_c \equiv 1 - \alpha_c$  ( $\Phi_c > 0$ ), which is  $\sim 0.01$  at  $t = 0$ . Here,  $\alpha_c$  denotes the central value of the lapse function. Since  $\Phi_c$  is approximately proportional to  $M/R$ ,  $\Phi_c^{-1}$  can be used as a measure of the characteristic length scale for the regridding. Typically, the value of  $N$  is chosen monitoring the magnitude of  $\Phi_c$  in the following manner; for  $\Phi_c \leq 0.04$ , we set  $N = 420$ ; for  $0.04 \leq \Phi_c \leq 0.1$ , we set  $N = 700$ ; for  $0.1 \leq \Phi_c \leq 0.2$ , we set  $N = 1200$ ; and for  $0.2 \leq \Phi_c$ , we set  $N = 1800$ , and keep this number until the termination of the simulations. Note that at  $t = 0$ , the equatorial radius is covered by 400 grid points in this case. With this setting, the total discarded fraction of the baryon rest-mass which is located outside new regridded domains is  $\lesssim 1\%$ . The grid spacing in  $N = 1800$  is  $\sim 0.6$  km for differentially rotating initial condition and  $\sim 0.6$ – $0.8$  km for rigidly rotating cases. A previous work [12] illustrates that with these grid resolutions a convergent result is obtained for most cases.

Nevertheless, we should be very careful in judging black hole formation since the criterion for the black hole formation near a threshold depends sensitively on the strength of shocks that are formed when the density around the central region exceeds  $\rho_{\text{nuc}}$ . The shocks in numerical simulations in general become stronger with improving the grid resolutions. This implies that a black hole may be spuriously formed in a coarse grid resolution in which the strength of the shocks is underestimated. To avoid such misjudging, in the case that a black hole is likely to be formed, we perform simulations with a finer grid resolution as follows; for  $\Phi_c \leq 0.04$ , we set  $N = 620$ ; for  $0.04 \leq \Phi_c \leq 0.1$ , we set  $N = 1020$ ; for  $0.1 \leq \Phi_c \leq 0.2$ , we set  $N = 1700$ ; and for  $0.2 \leq \Phi_c$ , we set  $N = 2500$ . Note that at  $t = 0$ , the equatorial radius is covered by 600 grid points in this case. If we find a convergent result on the black hole formation in both resolutions, we judge that the black hole is formed.

Simulations for each model with the typical grid resolution are performed for 40,000–50,000 time steps. The required CPU time for one model is about 20 hours using 4 processors of FACOM VPP5000 at the data processing center of National Astronomical Observatory of Japan, and about 10 hours using 8 processors of NEC SX6 at the data processing center of ISAS in JAXA.

### C. Method of three-dimensional simulation

Since computational resources are restricted and we cannot take the grid number per one direction as large as that in the axisymmetric case, it is not a good idea to perform three-dimensional simulations from the initial conditions with  $\rho_{\text{max}} = 10^{10}$  g/cm<sup>3</sup>. To save computational time, we always follow the early stage of the collapse using the axisymmetric code. After the collapse proceeds sufficiently, we change to the three-dimensional code. In preparing the initial conditions of three-dimensional computations, numerical results of the axisymmetric simulations are used. In the early stage of collapse at which the value of  $\beta$  of the collapsing star is not still very large ( $\lesssim 0.2$ ), nonaxisymmetric dynamical instabilities will not be induced. For highly differentially rotating cases, nonaxisymmetric instabilities could be induced even with a low value of  $\beta$  [28]. However in such cases, the growth time of the nonaxisymmetric instabilities would be much longer than the collapse time scale [28]. Therefore, the method that we adopt is appropriate.

Specifically, the initial condition for the three-dimensional simulations is prepared when the central value of the lapse function becomes  $\alpha_c = 0.8$  in the axisymmetric simulations. (For some case in which the minimum value of  $\alpha_c$  is slightly larger than 0.8, we choose the value as 0.85.) Since our major purpose in the three-dimensional simulations is to investigate the nonaxisymmetric dynamical stability of the collapsing star, we add a nonaxisymmetric density perturbation to the axisymmetric state. Associated with this change, the metric should be also perturbed, but we do not know how to do. For this reason, we adopt a very simple method for setting the initial conditions as follows.

First, we note that for  $\alpha_c \geq 0.8$ , the magnitude of  $\tilde{\gamma}_{ij} - \delta_{ij}$  is very small ( $\ll 0.01$ ) for all the components, and hence, the spatial hypersurface is approximately conformally flat. Also, the trace of the extrinsic curvature is nearly equal to zero because of our choice of the slicing condition. Thus, in setting the initial conditions of the three-dimensional simulations, we assume that the three-hypersurface is conformally flat and  $K_k^k = 0$  for simplicity. Then, we determine the conformal factor and the trace-free extrinsic curvature using the constraint equations. In this case, for a solution of the constraint equations, we only need to extract  $\rho_*$ ,  $\hat{e}$ , and  $\hat{u}_i$  from the numerical results of the axisymmetric simulations in the following method.

In the first step, we solve the momentum constraint equation using the York's procedure [54]. Setting

$$\hat{A}_{ij} \equiv \tilde{A}_{ij}\psi^6 = \partial_i W_j + \partial_j W_i - \frac{2}{3}\delta_{ij}\partial_k W_k, \quad (50)$$

where  $W_k$  is a three-vector, the momentum constraint is written as

$$\Delta_{\text{flat}} W_i + \frac{1}{3}\partial_i \partial_j W_j = 8\pi\rho_* \hat{u}_i, \quad (51)$$

where  $\Delta_{\text{flat}}$  is the flat Laplacian. Since  $\rho_*$  and  $\hat{u}_i$  are given, this equation is solved by a standard procedure (e.g., [13]) to give the tracefree part of the extrinsic curvature.

In the next step, the Hamiltonian constraint equation is solved. In the conformally flat spatial hypersurface, the equation for the conformal factor  $\psi$  is written as

$$\Delta_{\text{flat}}\psi = -2\pi\rho_*\hat{e}\psi^{-1} - \frac{\psi^{-7}}{8}\hat{A}_{ij}\hat{A}^{ij}. \quad (52)$$

Since  $\rho_*$  and  $\hat{e}$  were given, and  $\hat{A}_{ij}$  was already computed in the first step,  $\psi$  is also computed by a standard procedure often used in the initial value problem.

The simulations were performed using a fixed uniform grid and assuming reflection symmetry with respect to the equatorial plane. The typical grid size is  $(2N + 1, 2N + 1, N + 1)$  for  $(x, y, z)$ , and we adopt  $N = 156, 188,$  and  $220$ . The grid covers the region  $-L \leq x \leq L, -L \leq y \leq L,$  and  $0 \leq z \leq L$  where  $L$  is the location of the outer boundaries along each axis. For a given model, we take the identical value of  $L$  irrespective of the value of  $N$ . The grid spacing  $\Delta x = L/N$  is chosen to be larger than that adopted in the corresponding axisymmetric simulation because of restricted computational resources for the three-dimensional case. In the case of  $N = 156$ , we choose the grid spacing twice as large as that of the corresponding axisymmetric simulations. The typical computation is performed with  $N = 188$ , and to check the convergence, the value of  $N$  is varied. For models in which a bar-mode instability sets in, simulations are performed with  $N = 220$ .

The value of  $L$  is much smaller than that of the axisymmetric simulation. This implies that we discard the matter located in the outer region of the collapsing core. Specifically, we discarded the matter outside a sphere of radius  $\approx r_0$  by the rule

$$\rho_*(\text{new}) = \rho_*(\text{axisymmetric}) \times \frac{1}{e^{(r-r_0)/\delta r} + 1}, \quad (53)$$

where  $r_0 \approx 0.95L$  and  $\delta r = 2\Delta x$ . In this method, the fraction of the discarded baryon mass located for  $r > r_0$  is about 10–20% (compare Tables II and IV).

In this paper, we focus primarily on the dynamical stability against  $m = 2$  bar-mode deformation, since it is expected to be the fastest growing mode. Specifically, we superimpose a density perturbation in the form

$$\rho_* = \rho_*(\text{new}) \left( 1 + 0.4 \frac{x^2 - y^2}{L^2} \right). \quad (54)$$

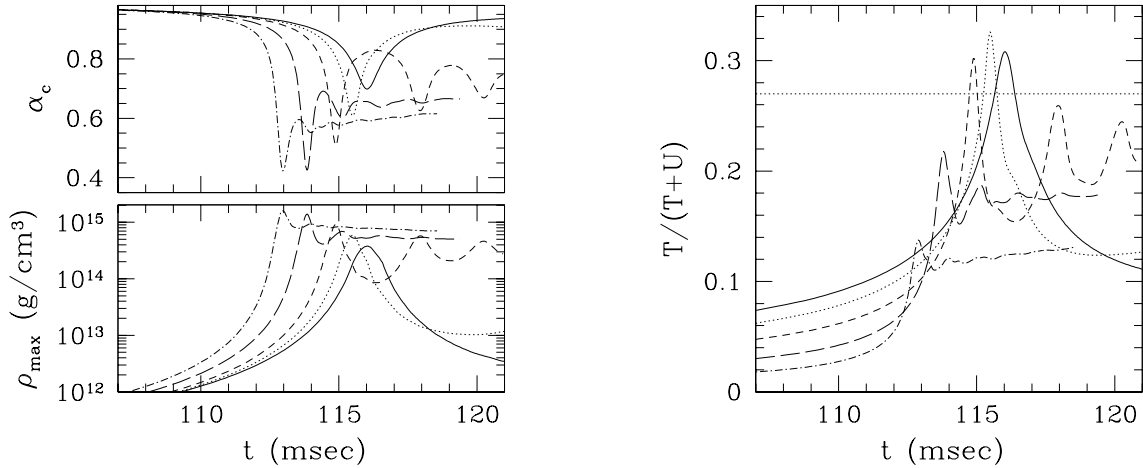
To check that the bar-mode perturbation grows for dynamically unstable models even when the initial configuration is nearly axisymmetric, we also performed simulations without adding nonaxisymmetric perturbation besides random numerical noises for selected unstable models. We found that in such cases, the bar-mode perturbation indeed grows although it takes more computational time to follow the growth.

In the case that the equations of state are very soft, the degree of the differential rotation is very high, and the value of  $\beta$  is large enough ( $\gtrsim 0.14$ ) for a collapsed star,  $m = 1$  modes may grow faster than the  $m = 2$  mode [55,56]. In the formation of neutron stars in which  $\rho_{\text{max}} > \rho_{\text{nuc}}$ , the equation of state is stiff, and hence, the  $m = 1$  mode may not be very important. On the other hand, in the formation of oscillating stars, equations of state can be soft for  $\rho_{\text{max}} < \rho_{\text{nuc}}$ . However, the value of  $\beta$  in such phase of subnuclear density are not very large. Thus, it is expected that even if the  $m = 1$  mode becomes unstable, the perturbation may not grow as significantly as found in [55,56]. Hence, we do not pay particular attention to this mode in this paper. Since nonaxisymmetric numerical noises are randomly included at  $t = 0$ , in some models, the  $m = 1$  mode grows as found in Sec. V. However, the amplitude of the perturbation is indeed not as large as that for  $m = 2$ .

Since we assume the conformal flatness in spite of the fact that the conformal three-metric is slightly different from zero in reality, a small systematic error is introduced in setting the initial data. Moreover, we discard the matter located in the outer region of the collapsing core according to Eq. (53). This could also introduce a systematic error. To confirm that the magnitude of such error induced by these approximate treatments is small, we compare the results in the three-dimensional simulations with those in the axisymmetric ones. We have found that the results agree well each other and the systematic error is not very large. This will be illustrated in Sec. V (cf. Fig. 13).

Simulations for each model with the grid size (441, 441, 221) ( $N = 220$ ) were performed for about 15,000 time steps. The required CPU time for computing one model is about 30 hours using 32 processors of FACOM VPP 5000 at the data processing center of National Astronomical Observatory of Japan.

#### IV. NUMERICAL RESULTS OF AXISYMMETRIC SIMULATIONS



(a) (b)  
 FIG. 1. Evolution of (a)  $\alpha_c$  and  $\rho_{\max}$  and (b)  $\beta = T/(T+U)$  for models M7c1 (solid curve), M7c2 (dotted curve), M7c3 (dashed curve), M7c5 (long-dashed curve), and M7c6 (dotted-dashed curve). The dotted horizontal line denotes  $\beta = 0.27$ .

#### A. Outcomes

In the last column of Table II, we summarize the outcomes of stellar core collapse in the axisymmetric simulations for  $\Gamma_1 = 1.3$  and  $\Gamma_2 = 2.5$ . They are divided into three types: Black hole, neutron star, and oscillating star for which the maximum density inside the star is not always larger than  $\rho_{\text{nuc}}$ . For given values of  $K_0 (\geq 7 \times 10^{14} \text{ cgs})$  and  $A$ , a black hole is formed when the initial value of  $\beta$  (hereafter  $\beta_{\text{init}}$ ) is smaller than critical values that depend on  $A$ . As described in Sec. III A,  $\beta$  in the collapse is defined by

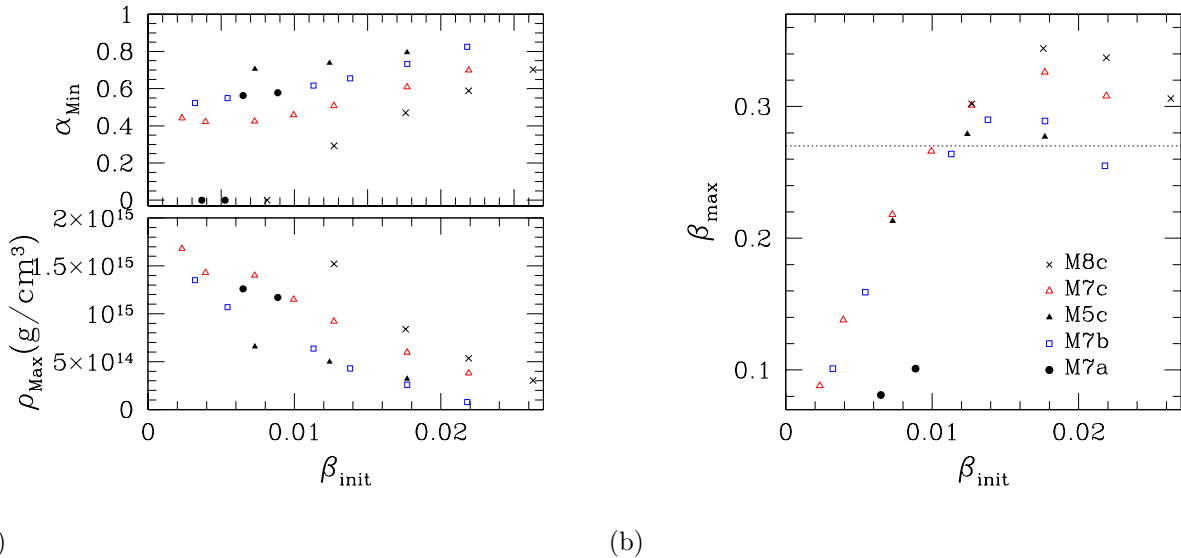
$$\beta \equiv \frac{T}{T+U}. \quad (55)$$

In the dynamical spacetime with  $M_* \approx M$  for  $\Gamma = 4/3$ ,  $W$  would be approximately written as

$$W \approx U + T + T_{\text{other}}, \quad (56)$$

where  $T_{\text{other}}$  denotes a partial kinetic energy obtained by subtracting the rotational kinetic energy from the total. Thus,  $T/W$  should be approximated by  $T/(U + T + T_{\text{other}})$ , but we do not know how to appropriately define  $T_{\text{other}}$ . Fortunately, it would be much smaller than  $T$  at the initial state, at the maximum compression at which the spin of the collapsing star becomes maximum, and in a late phase when the outcome relaxes to a quasistationary state. This implies that using the definition of (55), the maximum value and a final relaxed value of  $\beta$  will be computed approximately. In other phases,  $\beta$  computed by Eq. (55) gives an overestimated value.

In Fig. 1, we show the evolution of the central value of the lapse function ( $\alpha_c$ ), the maximum value of the density ( $\rho_{\max}$ ), and  $\beta$  for models M7c1, M7c2, M7c3, M7c5, and M7c6. In the following, we denote the maximum density and minimum value of the lapse achieved in the whole evolution as  $\rho_{\text{Max}}$  and  $\alpha_{\text{Min}}$ , respectively. On the other hand, the maximum density at a given time is denoted by  $\rho_{\max}$ .



(a) (b)  
 FIG. 2. (a)  $\alpha_{\text{Min}}$  and  $\rho_{\text{Max}}$  and (b)  $\beta_{\text{max}}$  for various values of  $\beta_{\text{init}}$ . In both panels, the solid triangle, the solid circles, open squares, open triangles, and crosses denote models M5c, M7a, M7b, M7c, and M8c, respectively. The dotted line in panel (b) denotes  $\beta_{\text{max}} = 0.27$ .

Figure 1 shows that for most cases, the value of  $\rho_{\text{Max}}$  becomes larger than  $\rho_{\text{nuc}}$ . However, with the increase of  $\beta_{\text{init}}$ , it decreases significantly. Also, for several cases,  $\rho_{\text{max}}$  drops below  $\rho_{\text{nuc}}$  soon after it reaches the maximum. Such oscillating stars for which the values of  $\rho_{\text{max}}$  oscillate between  $\rho_1 (> \rho_{\text{nuc}})$  and  $\rho_2 (< \rho_{\text{nuc}})$  are referred to type O-A in Table II. On the other hand, if  $\beta_{\text{init}}$  is not very large and neither is the maximum value of  $\beta$  (hereafter  $\beta_{\text{max}}$ ), a neutron star or a black hole is formed. Here, formation of a neutron star implies that  $\rho_{\text{max}}$  achieved after the stellar collapse is always larger than  $\rho_{\text{nuc}}$ . Formation of a black hole implies that we confirm the formation of apparent horizon.

In Figs. 2(a) and (b), we show  $\alpha_{\text{Min}}$ ,  $\rho_{\text{Max}}$ , and  $\beta_{\text{max}}$  for various values of  $\beta_{\text{init}}$ . For  $\beta_{\text{init}} \gtrsim 0.02$  with  $K_0 = 7 \times 10^{14}$  cgs,  $\rho_{\text{Max}}$  is smaller than  $\rho_{\text{nuc}}$ , and the resulting star is quasiradially oscillating with the subnuclear density. Such stars are referred to as O-B in Table II.

Figure 1 and Table II show that initial high degrees of differential rotation with  $A = 0.25$  and  $0.1$  have an effect for preventing black hole formation. (Compare the parameters among the models with  $K_0 = 7 \times 10^{14}$  cgs.) For the rigidly rotating cases, the stars with  $\beta_{\text{init}} \lesssim 0.005$  collapse to a black hole. On the other hand, the stars with  $\beta_{\text{init}} \sim 0.003$  do not collapse to a black hole but form a neutron star for  $A = 0.1$  and  $0.25$ . This is simply because the stars with such high degrees of differential rotation have a large centrifugal force near the rotational axis, and hence, even in the case that the global value  $\beta_{\text{init}}$  is small, the effective local value of the centrifugal force would be large enough to prevent cores from collapsing to a black hole.

## B. Evolution of $\beta$ for $\Gamma_1 = 1.3$ and $\Gamma_2 = 2.5$

Figures 1 and 2 indicate that with the increase of  $\beta_{\text{init}}$ ,  $\alpha_{\text{Min}}$  ( $\rho_{\text{Max}}$ ) increases (decreases). The value of  $\beta_{\text{max}}$  is larger for the larger value of  $\beta_{\text{init}}$  as far as  $\beta_{\text{init}} \lesssim 0.02$ . However, the amplification factor  $\beta_{\text{max}}/\beta_{\text{init}}$  is smaller for the larger value of  $\beta_{\text{init}}$ . This is because in the collapse with the large values of  $\beta_{\text{init}}$ , strong centrifugal force prevents the maximum value of compactness (or maximum density or maximum value of the gravitational potential) from being increased by a large factor. Spin can be increased by a larger factor for a star which gains a larger compactness. Therefore, for stars of approximately identical mass, the amplification factor  $\beta_{\text{max}}/\beta_{\text{init}}$  should be smaller for the larger value of  $\beta_{\text{init}}$ .

The typical value of  $\beta_{\text{max}}/\beta_{\text{init}}$  is 10–20 for rigidly rotating case and for differentially rotating cases with  $\beta_{\text{init}} \gtrsim 0.015$ . Naive estimation predicts that  $T \propto J^2/(MR^2)$  and  $W \propto M^2/R$ , and hence,  $\beta \propto J^2/(M^3R)$ . Thus,  $\beta$  seems to be proportional to the inverse of the stellar radius in the condition that the mass and the angular momentum of the system are conserved. Since the characteristic stellar radius changes by a factor of  $\sim 100$  during the collapse, we may predict that  $\beta$  also increases by two orders of magnitude. However, this does not occur. The reason for the

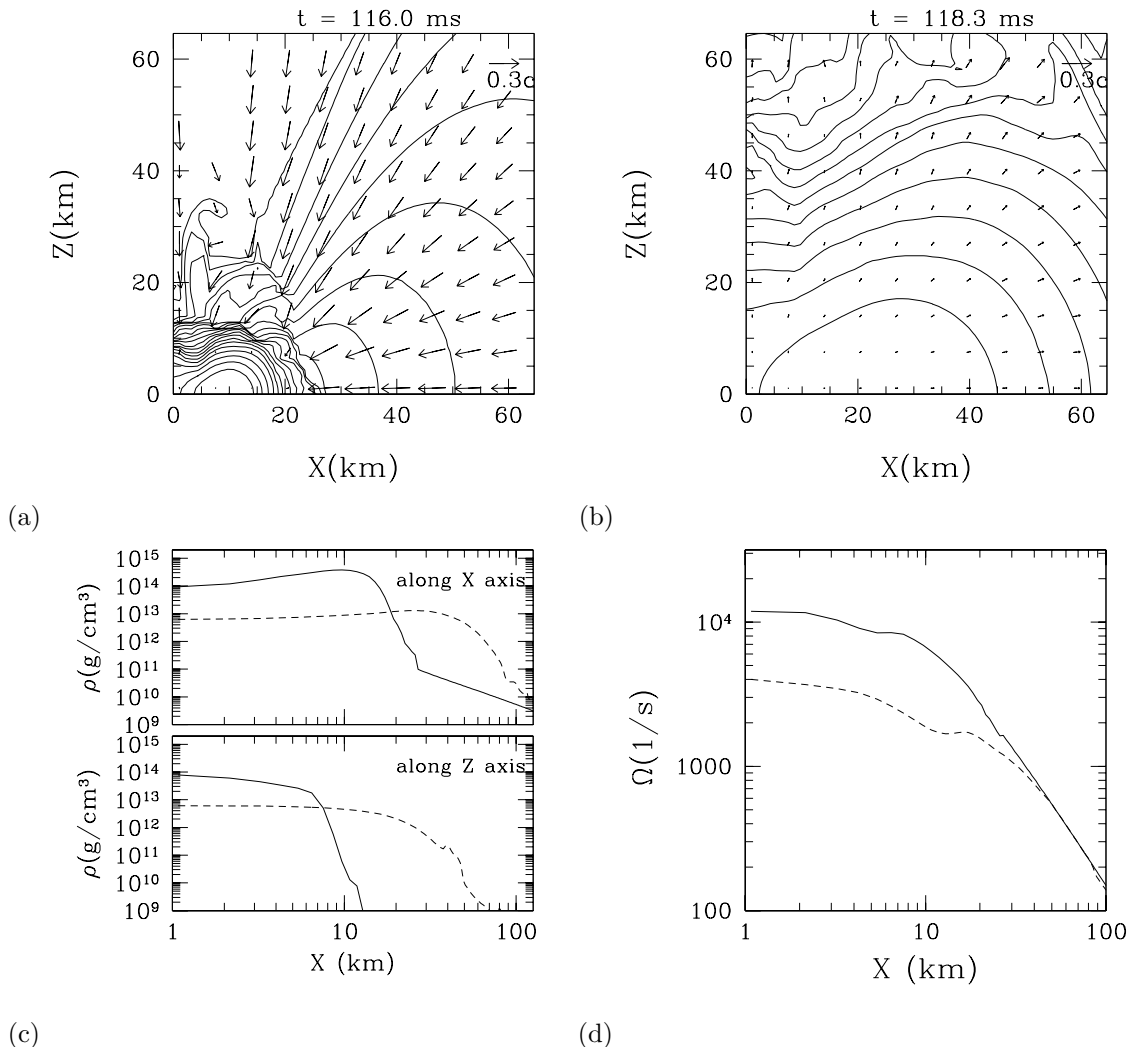


FIG. 3. (a) and (b): The density contour curves for  $\rho$  for model M7c1 at  $t = 116.0$  and  $118.3$  msec. The solid contour curves are drawn for  $\rho/\rho_{\max} = e^{-0.3j}$  for  $j = 1, 2, 3, \dots, 20$  where  $\rho_{\max}$  denotes the maximum of  $\rho$  at the given times, which are found from Fig. 1(a). Vectors indicate the local velocity field ( $v^x, v^z$ ), and the scale is shown in the upper right-hand corner. (c) Density profiles along the  $x$  and  $z$  axes at  $t = 116.0$  (solid curve) and  $118.3$  msec (dashed curve). (d) The same as (c) but for angular velocity along the radial coordinate in the equatorial plane.

rigidly rotating case is that although the core radius decreases to  $\sim 10$  km in the collapse, the outer region of the star which possesses a large fraction of the angular momentum does not collapse to such a small radius due to the strong centrifugal force. The reason for the highly differentially rotating cases with a high value of  $\beta_{\text{init}} \gtrsim 0.015$  is that the centrifugal force near the rotational axis is so strong that the collapse is halted before the stellar radius becomes  $\sim 10$  km. For low values of  $\beta_{\text{init}} \lesssim 0.01$ , the rotational velocity in the outer region is small, and also, the centrifugal force in the central region is not as strong as that for  $\beta_{\text{init}} \gtrsim 0.015$ . As a result, the stellar components that enclose a large fraction of the angular momentum can collapse to small radii, and hence,  $\beta$  can increase by a factor of  $\gtrsim 30$ .

For given values of  $K_0$  and  $\beta_{\text{init}}$ , the value of  $\beta_{\text{max}}$  is larger for higher degrees of differential rotation. This suggests that stellar cores with a higher degree of differential rotation may be more subject to nonaxisymmetric dynamical instabilities. For the identical value of  $\beta_{\text{init}}$ ,  $\beta_{\text{max}}$  is larger for higher-mass stellar cores with a larger value of  $K_0$  in the case of highly differentially rotating cores. (Compare, e.g., the solid triangle, the open triangle, and the cross in Fig. 2(b); more specifically, compare the results for models M5c1, M7c2, and M8c3, for which the values of  $\beta_{\text{init}}$  are approximately the same as 0.0177, but  $\beta_{\text{max}}$  is larger for larger mass.) The reason for this behavior is that the stars of higher mass can reach a more compact state during the collapse, and as a result, their spins can be increased by a larger factor and so can be  $\beta$ . On the other hand, for rigidly rotating cases, this feature is not very outstanding.

An interesting point is that the value of  $\beta_{\text{max}}$  has a maximum around  $\beta_{\text{init}} \sim 0.018$  for  $A = 0.1$  and  $0.25$ : For

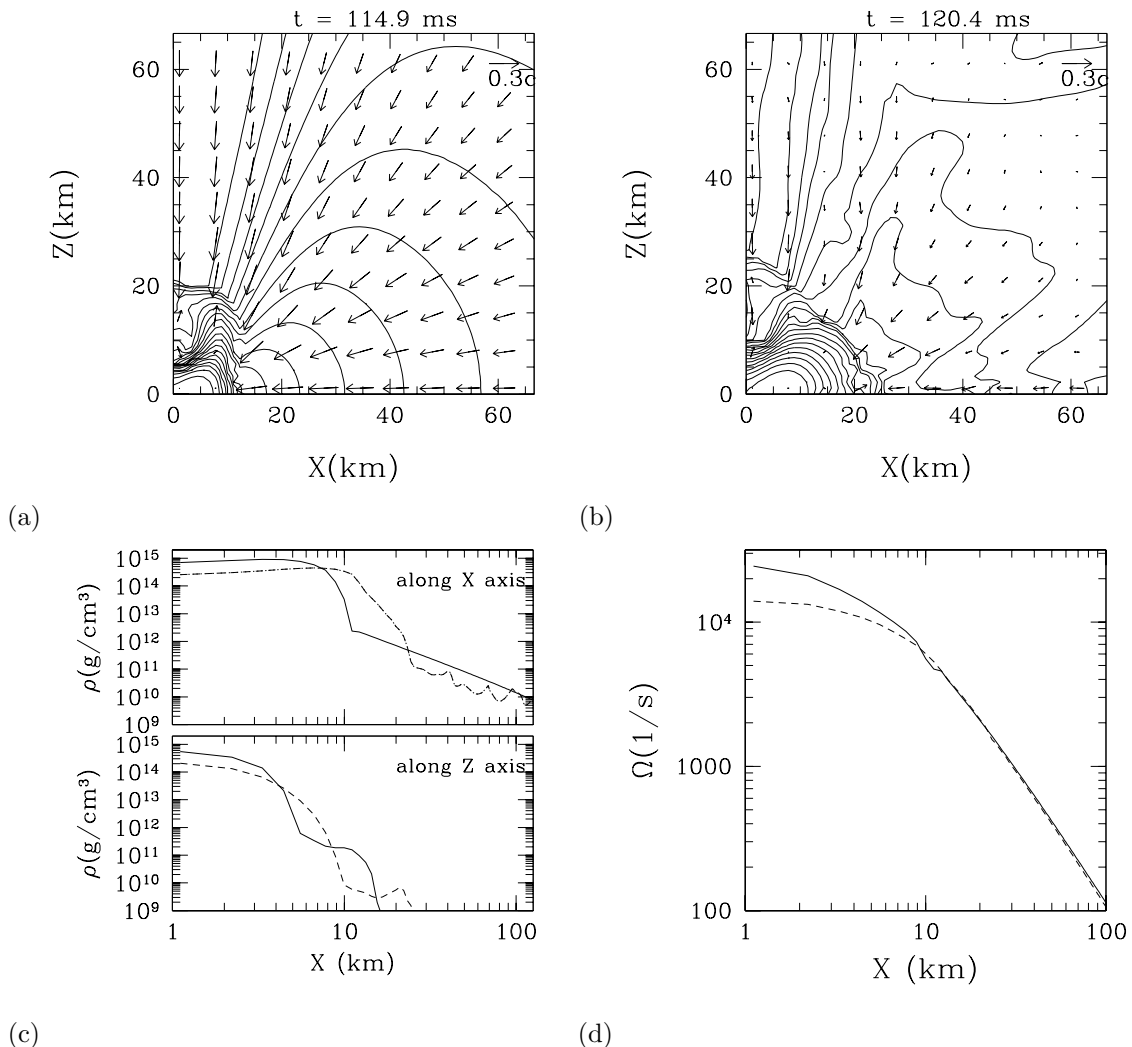


FIG. 4. The same as Fig. 3(a)–(d) but for model M7c3 at  $t = 114.9$  and  $120.4$  msec. The solid and dashed curves in panels (c) and (d) are drawn for the corresponding time slices, respectively.

$\beta_{\text{init}} \lesssim 0.018$ ,  $\beta_{\text{max}}$  is an increase function of  $\beta_{\text{init}}$ , reflecting the initial magnitude of the spin. However, for  $\beta_{\text{init}} \gtrsim 0.018$ ,  $\beta_{\text{max}}$  is a decrease function. The reason is that the centrifugal force of the rotating stars with  $\beta_{\text{init}} \gtrsim 0.018$  is so strong that the collapse is halted before the stellar core becomes compact enough. This feature is also reflected in Fig. 2(a) from which we find that the value of  $\alpha_{\text{Min}}$  is an increase function of  $\beta_{\text{init}}$ .

As reviewed in Sec. I, nonaxisymmetric dynamical instabilities of *rotating stars in equilibrium* set in when the value of  $\beta$  becomes larger than  $\sim 0.27$ . If we assume that the collapsing stars with  $\beta_{\text{max}} \gtrsim 0.27$  are dynamically unstable, Fig. 2(b) suggests that the conditions for the onset of the instabilities will be the following: (i) the progenitor of the collapse should be highly differentially rotating with  $A \lesssim 0.25$ ; (ii) the progenitor has to be moderately rapidly rotating with  $0.01 \lesssim \beta_{\text{init}} \lesssim 0.02$ ; (iii) the progenitor star has to be massive enough.

However, it should be kept in mind that the condition  $\beta_{\text{max}} > 0.27$  is satisfied only for a few msec during the stellar collapse. This indicates that if the growth time scale of nonaxisymmetric instabilities is not as short as a few msec, the system may remain nearly axisymmetric. Thus, the condition  $\beta_{\text{max}} \gtrsim 0.27$  does not have to be the criterion for the onset of nonaxisymmetric dynamical instabilities in dynamical systems. The examples are shown in Sec. V.

### C. Profiles of density and angular velocity for $\Gamma_1 = 1.3$ and $\Gamma_2 = 2.5$

In [21], Tohline and Hachisu illustrated that the stars with toroidal density profiles are dynamically unstable against a bar-mode perturbation even if  $\beta$  is much smaller than 0.27. Also in [28], we indicated that not only the value of  $\beta$

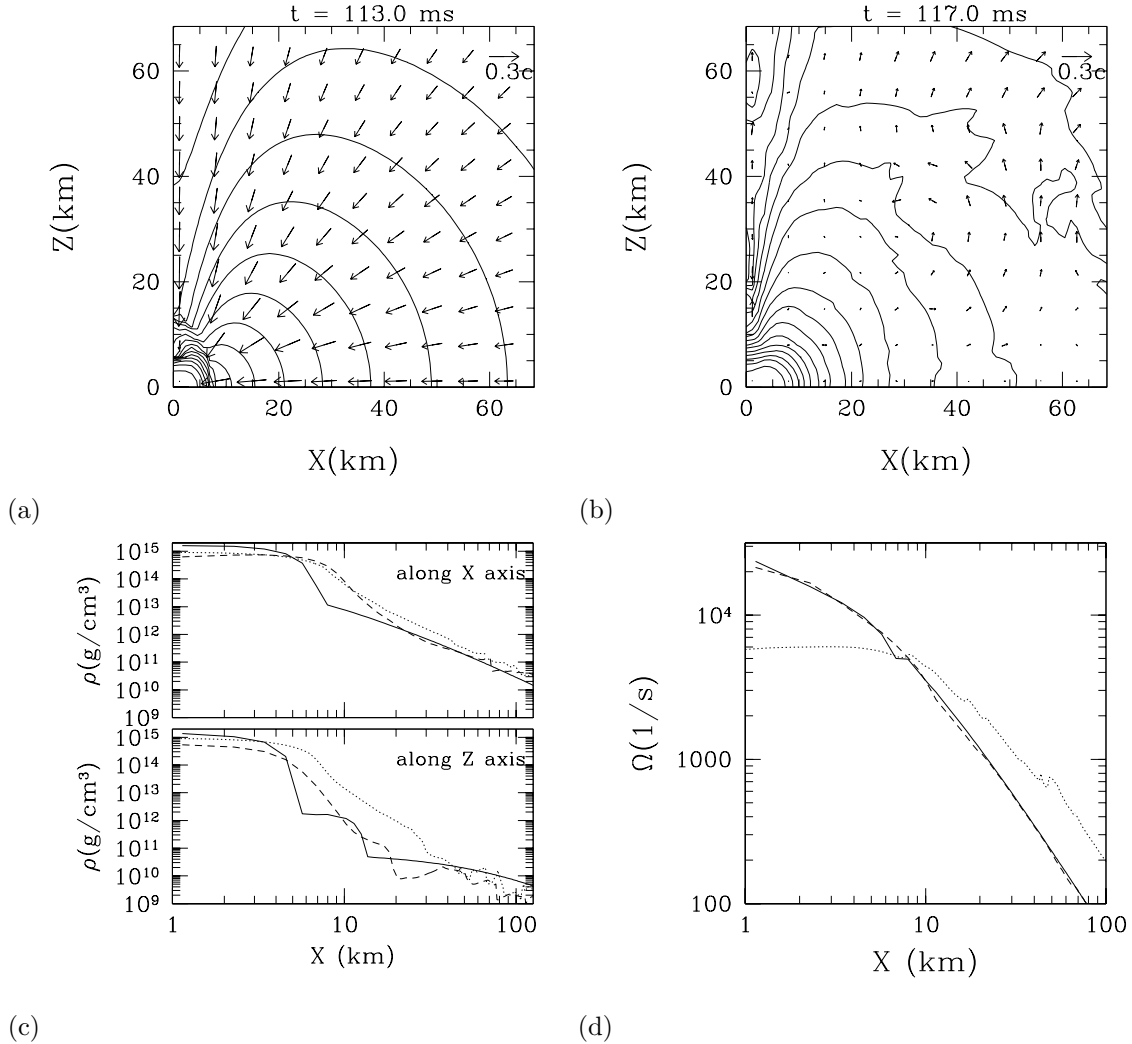


FIG. 5. The same as Fig. 3(a)–(d) but for model M7c6 at  $t = 113.0$  and  $117.0$  msec. The solid and dashed curves in panels (c) and (d) are drawn for the corresponding time slices, respectively. For comparison, the results for model M7a2 at  $t = 121.3$  msec are shown (dotted curves).

but also the degree of differential rotation is a key parameter for determining nonaxisymmetric stability of rotating stars. Thus, here, we focus on the profiles of the density and the rotational angular velocity of the outcomes in the stellar collapse.

In Figs. 3–5, we display the snapshots of the density contour curves, velocity vectors in the  $x$ - $z$  plane, density profiles along  $x$  and  $z$  axes, and rotational angular velocity profiles as a function of the radial coordinate in the equatorial plane at the time slices that the maximum completion is achieved and the system relaxes to an approximately quasistationary state for models M7c1, M7c3, and M7c6. These figures clarify how the outcomes are changed with the varying  $\beta_{\text{init}}$  for (approximately) identical values of  $A$  and  $M$ . Panels (a), (b), and (c) show that for the larger values of  $\beta_{\text{init}}$ , the shape of the outcome is more torus-like. Numerical studies for nonaxisymmetric dynamical instabilities in rapidly rotating stars in equilibrium have illustrated that torus-like stars are often unstable [21,22,28]. This indicates that the models such as M7c1–M7c3 in which torus-like structures are formed are candidates for the onset of nonaxisymmetric dynamical instabilities even when the value of  $\beta$  is smaller than  $\sim 0.27$ .

The panels (d) in Figs. 3–5 show that all the outcomes of the collapse are differentially rotating. The degree of the differential rotation is very large for the cylindrical radius  $\varpi \gtrsim 10$  km as  $\Omega \propto \varpi^{-\delta}$  with  $\delta \sim 1.9$ – $2.0$ , reflecting the initial profile. In the inner region of  $\varpi \lesssim 10$  km, the rotational angular velocity does not change as steeply as that for  $\varpi \gg 10$  km. This also seems to reflect the initial rotational velocity profile for which  $\Omega$  is nearly constant for  $\varpi \lesssim \varpi_d$ . However, except for the very inner region, the star is totally differentially rotating, in particular in the outer region, for any models of  $A = O(0.1)$ . The results indicate that the initial rotational velocity profile is reflected

Model	$\Gamma_1$	$\Gamma_2$	$\alpha_{\text{Min}}$	$\rho_{\text{Max}}$	$\beta_{\text{max}}$	Outcome
M5c1A	1.3	2.5	0.79	3.2e14	0.28	O-A
M5c1C	1.28	2.75	0.80	3.8e14	0.33	O-A
M5c2A	1.3	2.5	0.74	5.0e14	0.28	O-A→NS
M5c2C	1.28	2.75	0.77	5.2e14	0.31	O-A→NS
M7b3A	1.3	2.5	0.65	4.8e14	0.29	NS
M7b3B	1.32	2.25	0.71	2.8e14	0.23	O-A
M7b3C	1.28	2.75	0.70	5.3e14	0.29	NS
M7c2A	1.3	2.5	0.61	6.0e14	0.33	O-A
M7c2B	1.32	2.25	0.75	5.6e14	0.21	O-A
M7c2C	1.28	2.75	0.67	5.6e14	0.36	O-A→NS
M7c3A	1.3	2.5	0.51	9.2e14	0.30	NS
M7c3B	1.32	2.25	0.38	1.2e15	0.26	O-A
M7c3C	1.28	2.75	0.61	7.6e14	0.33	NS
M7c4A	1.3	2.5	0.46	1.2e15	0.27	NS
M7c4B	1.32	2.25	—	—	—	BH
M7c4C	1.28	2.75	0.59	8.7e14	0.30	NS
M8c2A	1.3	2.5	0.59	5.4e14	0.34	O-A
M8c2B	1.32	2.25	0.86	2.2e14	0.16	O-A
M8c2C	1.28	2.75	0.64	5.2e14	0.37	O-A
M8c4A	1.3	2.5	0.29	1.5e15	0.30	NS
M8c4C	1.28	2.75	0.51	9.4e14	0.34	NS

TABLE III. Numerical results with different values of  $\Gamma_1$  and  $\Gamma_2$  for selected models.

in the outcome. Thus, if the progenitor of the collapse is highly differentially rotating, the outcomes will be always so and, as a result, be candidates for the bar-mode dynamical instabilities [28].

In Figs. 5(c) and 5(d), we display together the profiles of the density and the rotational angular velocity for model M7a2 (dotted curves) at  $t = 121.3$  msec at which the outcome has already relaxed to a quasistationary state. Figure 5(c) shows that the outcome is a spheroid not a torus-like object (i.e., the central density is highest). This is a characteristic property in the collapse with rigidly rotating initial conditions [52]. Figure 5(d) shows that the rotational angular velocity in the inner region is approximately flat and thus the high-density part of the protoneutron star is approximately rigidly rotating. The outer region of  $\varpi \gtrsim 10$  km, on the other hand, is differentially rotating, but the rotational angular velocity falls off in proportional to  $\varpi^{-\delta}$  with  $\delta \sim 1.4$ – $1.5$ ; i.e., the profile is approximately that of Kepler’s law, and hence, the degree of differential rotation in this case is smaller than that for differentially rotating initial conditions. More details about the outcomes in the rigidly rotating initial conditions are found in [52].

From the density contour curves, it is found that for all the differentially rotating models, the column density integrated along the rotational axis is much smaller than that along the equatorial plane after shocks sweep the matter. Namely, a funnel is formed around the rotational axis even in the absence of a black hole. This is due to the facts that the total mass around the rotational axis is initially small because of a high degree of differential rotation for the initial condition and that the formed shocks are strongest around the rotational axis. A current popular model for the central engine of gamma-ray bursts is the so-called collapsar model [57]. To escape the baryon-loading problem for the fire-ball model [58], it is often required to form a funnel in the collapsar models. In their scenario, a rapidly rotating black hole is formed, and subsequently, a jet emitted along the rotational axis of the black hole ejects the matter. The present results suggest that a high degree of differential rotation for the progenitor of the stellar collapse helps making a funnel without relying on the formation of a rapidly rotating black hole and subsequent jets.

#### D. Dependence on equations of state

To clarify the dependence of the outcomes on the equations of state, we performed simulations varying  $\Gamma_1$  and  $\Gamma_2$  as listed in Table III for models M5c1, M5c2, M7b3, M7c2, M7c3, M7c4, M8c2, and M8c4. Here, we focus only on highly differentially rotating cases with  $A = 0.1$  and  $0.25$ . The details for the cases of rigid rotation and moderate degrees of differential rotation with  $A \sim 1$  are presented in [52]. As listed in Table I, we choose three sets of  $(\Gamma_1, \Gamma_2)$

as (i) (1.3, 2.5), (ii) (1.32, 2.25), and (iii) (1.28, 2.75). In the following, we will refer to the models with (i), (ii), and (iii) using the labels A, B, and C, e.g., as M5c1A, M5c1B, and M5c1C.

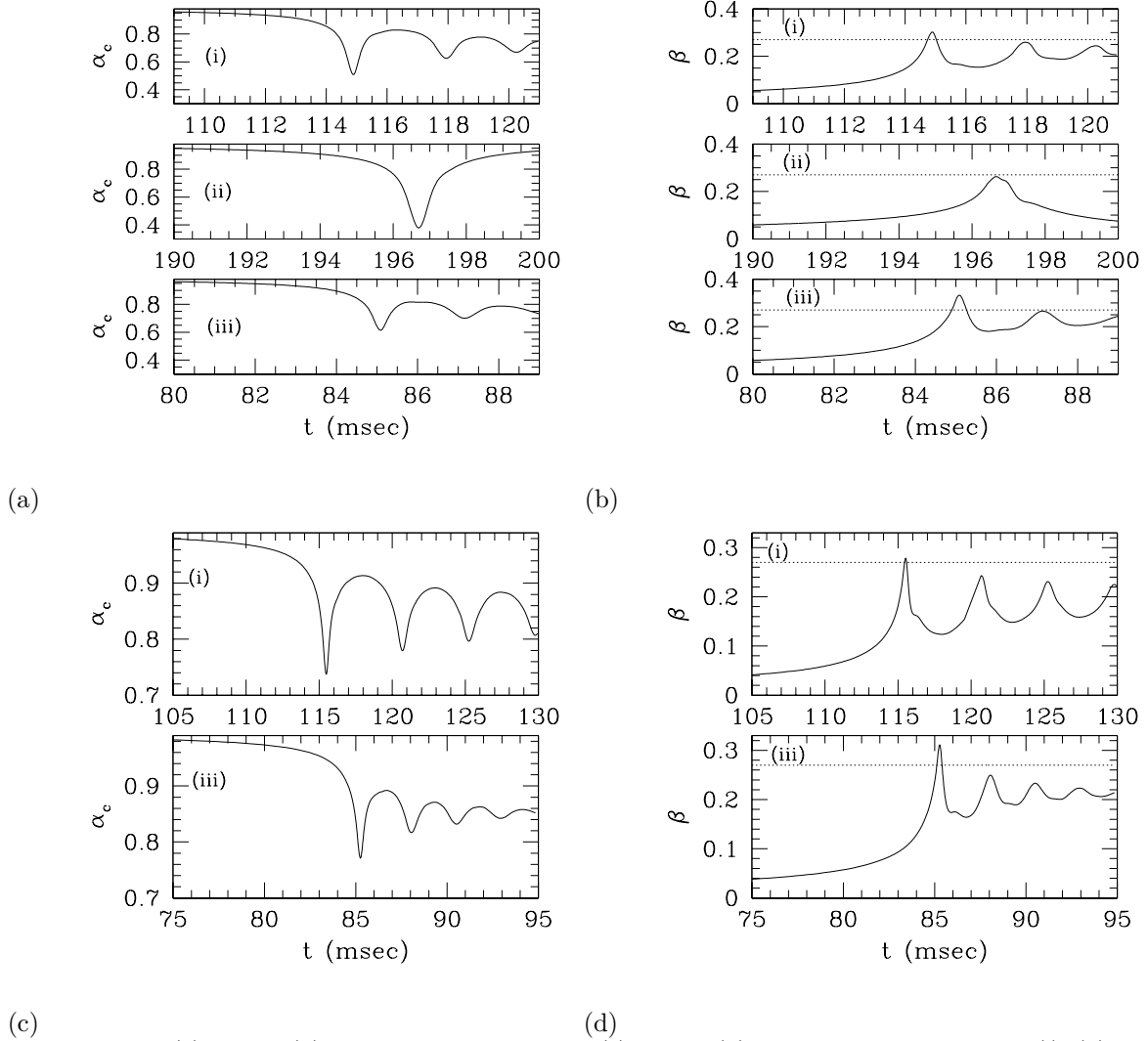


FIG. 6. Evolution of (a)  $\alpha_c$  and (b)  $\beta$  for model M7c3 and of (c)  $\alpha_c$  and (d)  $\beta$  for model M5c2. Panels (i), (ii), and (iii) are results for  $(\Gamma_1, \Gamma_2) = (1.3, 2.5)$ ,  $(1.32, 2.25)$ , and  $(1.28, 2.75)$ , respectively. The dotted horizontal lines in panels (b) and (d) denote  $\beta = 0.27$ .

In Fig. 6, we compare the evolutions of the central value of  $\alpha$  and  $\beta$  for models M7c3A, M7c3B, and M7c3C (Figs. 6(a) and (b)) and for M5c2A and M5c2C (Figs. 6(c) and (d)) as representative illustrations. In the previous section, we found that models M7c3 and M5c2 are possible candidates for the onset of nonaxisymmetric dynamical instabilities of  $\beta_{\max} > 0.27$ . Among these models of different equations of state,  $\beta_{\max}$  for case (iii) is largest. On the other hand,  $\beta_{\max}$  for case (ii) is much smaller than those in other two cases. This seems to be due to the fact that for smaller values of  $\Gamma_1$ , the depletion factor of the internal energy and the pressure in an early stage of collapse in which  $\rho \ll \rho_{\text{nuc}}$  is larger. As a consequence, the internal energy  $U$  is decreased to contribute to the increase of  $\beta$ , and furthermore, the matter around the rotational axis which possesses large values of the specific angular momentum collapses to a more compact state, for which a spin-up is enhanced effectively. On the other hand, the values of  $\alpha_c$  (compactness) for models M7c3C and M5c2C are larger (smaller) than that for M7c3A and M5c2A, respectively. This may be partly due to the fact that  $\Gamma_2$  for case (iii) is larger than that for (i), but mainly to the fact that the fraction of the matter which simultaneously collapses is smaller for case (iii) than for (i). This implies that to achieve a large value of  $\beta$ , it is not necessary for the whole system to become compact. Rather, essentially needed is to accumulate the matter with large values of the specific angular momentum in the central region. This point is reconfirmed from the results for M7c3B. In this case, the value of  $\beta_{\max}$  is much smaller than those for other two cases, although the

value of  $\alpha_c$  is smallest among three cases. This is due to the fact that in this case, a large fraction of the matter collapses nearly simultaneously independent of the magnitude of the specific angular momentum.

Table III also shows that the largest value of  $\beta_{\max}$  is achieved for case (iii) for all the initial conditions. This indicates that to achieve a large value of  $\beta$ , the depletion of the internal energy and the pressure in the early stage of the collapse, which in reality will be achieved by partial photo-dissociation of the iron to lighter elements and by the electron capture [48,49], should be sufficiently large to accelerate the collapse of the central region.

As indicated in Fig. 6, the outcomes for models M7c3 and M5c2 depend sensitively on the equations of state. For the small values of  $\Gamma_1$  (cases (i) and (iii)), an oscillating protoneutron star is formed eventually. The amplitude of the oscillation is smaller and the period is shorter for the smaller value of  $\Gamma_1$  (case (iii)). As a result, the protoneutron star relaxes to a quasistationary state more quickly. For a long period of the oscillation, the duration of the phase, in which  $\beta$  and rotational angular velocity remain small, becomes long. This also suggests that for the onset of nonaxisymmetric dynamical instabilities, the smaller value of  $\Gamma_1$  may be preferable.

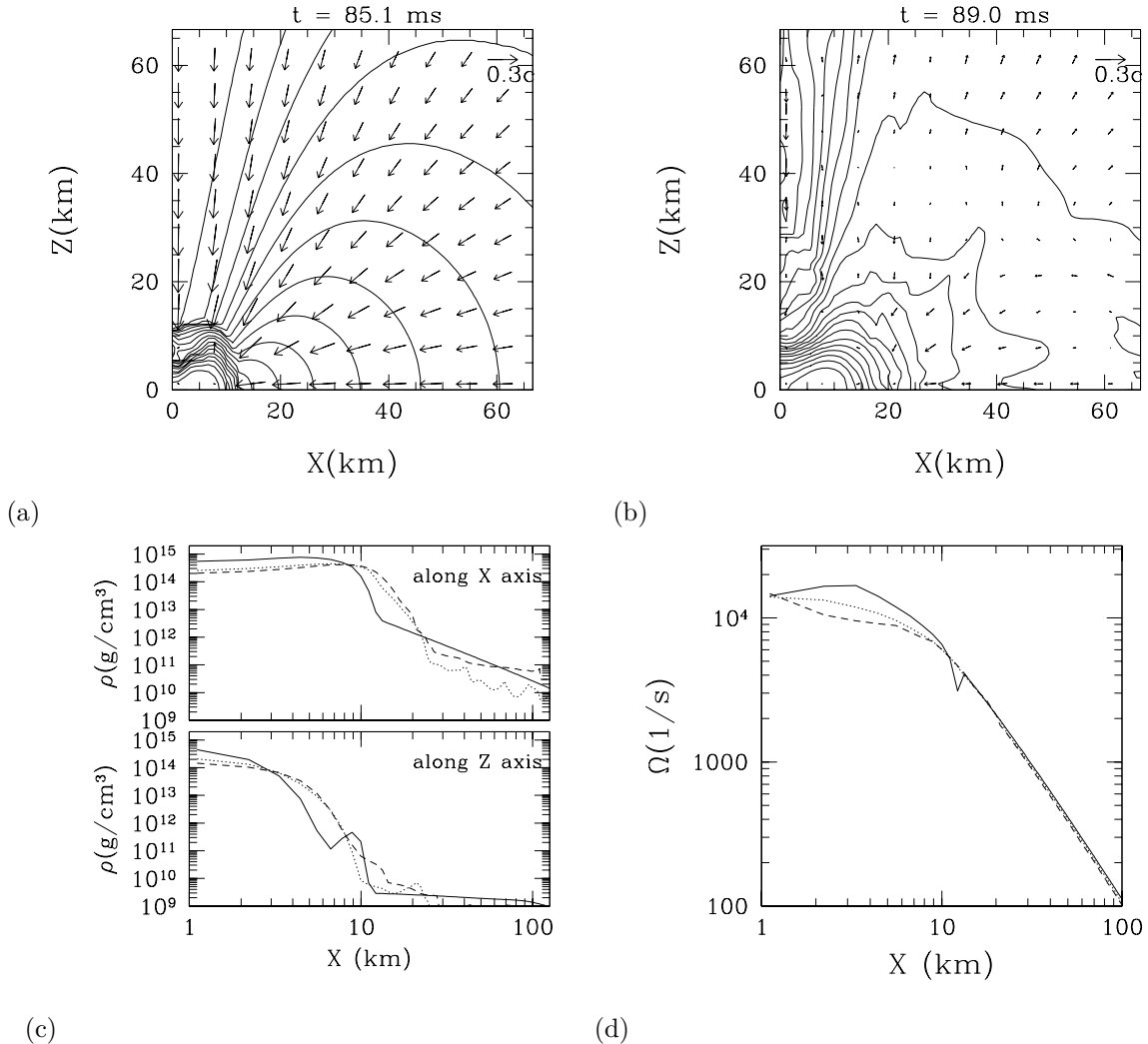


FIG. 7. The same as Fig. 3(a)–(d) but for model M7c3C at  $t = 85.1$  and  $89.0$  msec. The solid and dashed curves in panels (c) and (d) are drawn for the corresponding time slices, respectively. In panels (c) and (d), we plot the results for model M7c3A at  $t = 120.4$  msec (dotted curves) for comparison.

In Fig. 7, we display the snapshots of the density contour curves and the velocity vectors at the time slices that the maximum compression is achieved and the system relaxes to an approximately quasistationary state for model M7c3C. The density profiles and the angular velocity in the equatorial plane at the corresponding time steps are shown in panels (c) and (d) together with results for model M7c3A (displayed in Fig. 4). It is found that the shape of the outcome for M7c3C is more torus-like than that for M7c3A. In addition, the degree of differential rotation for M7c3C is slightly higher than that for M7c3A. These facts indicate that the outcome for M7c3C is likely to be more

subject to nonaxisymmetric dynamical instabilities. These properties depend weakly on the value of  $K_0$  (i.e., mass of the progenitor). Indeed, the outcome of M5c2C is more torus-like and the degree of differential rotation in the central region for M5c2C is higher than those for M5c2A. As illustrated in Sec. V, thus, the value of  $\Gamma_1$  is one of key parameters for determining the onset of nonaxisymmetric dynamical instabilities.

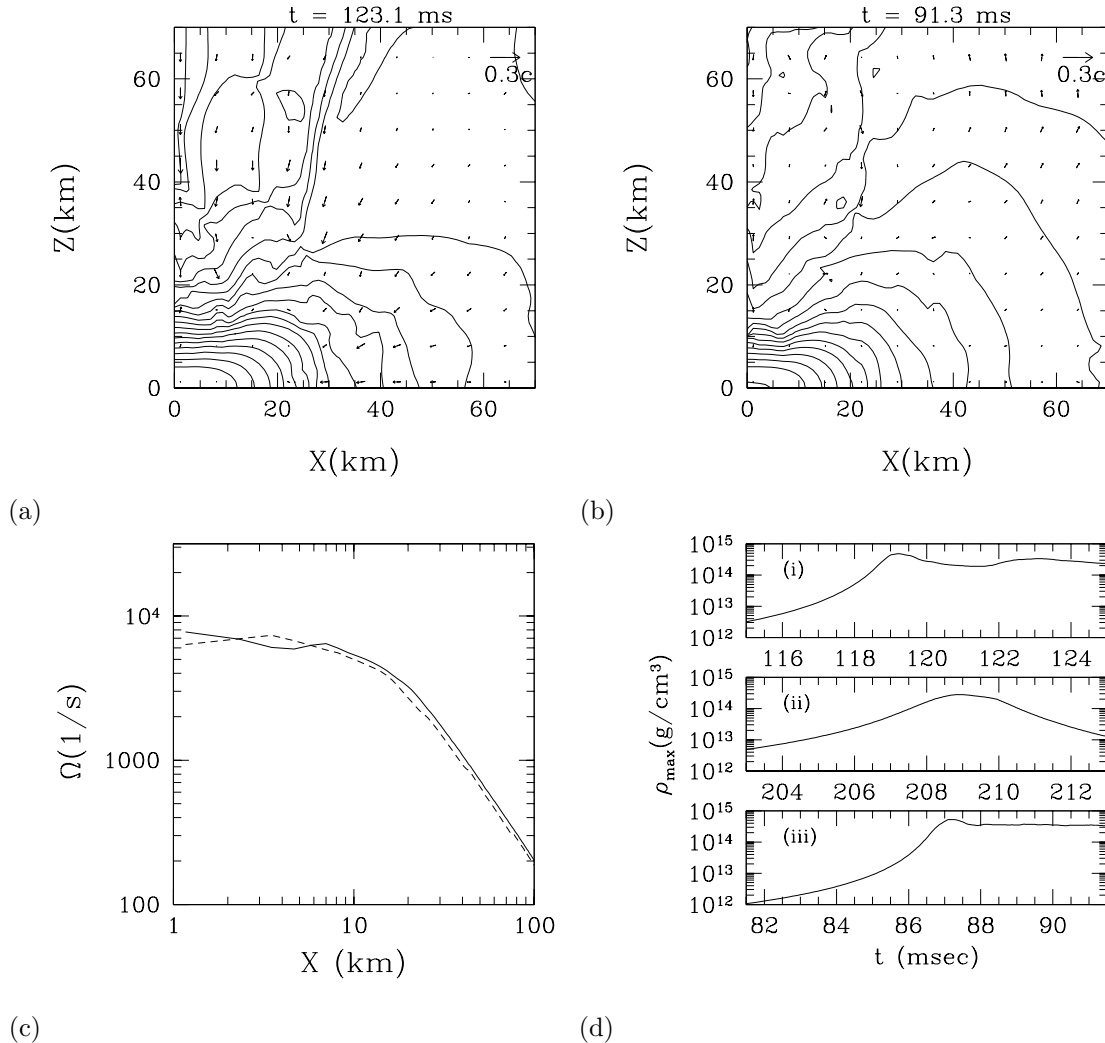


FIG. 8. (a) The density contour curves for  $\rho$  for model M7b3A at  $t = 123.1$  msec. The contour curves and vectors are drawn in the same method as in Fig. 3. (b) The same as panel (a) but for model M7b3C at  $t = 91.3$  msec. (c) Angular velocity along the radial coordinate in the equatorial plane for models M7b3A at  $t = 123.1$  msec (solid curve) and M7b3C at  $t = 91.3$  msec (dashed curve). (d)  $\rho_{\max}$  as a function of time for models M7b3A, M7b3B, and M7b3C.

We note that the properties pointed above is found only for  $A = 0.1$ . For  $A = 0.25$ , the value of  $\beta_{\max}$  for two equations of state (i) and (iii) are not very different. Also, the density profile and the angular velocity profile of the formed neutron stars are similar (see Fig. 8). This indicates that for large values of  $A$ , the larger depletion factor of the internal energy (smaller value of  $\Gamma_1$ ) in the early stage of the collapse does not play an important role for accumulating the matter of large specific angular momentum in the central region. This result suggests that the stability property against nonaxisymmetric deformation will not depend on the choice of  $\Gamma_1$  and  $\Gamma_2$  for  $A = 0.25$  as strongly as for  $A = 0.1$  as long as  $\Gamma_1 \leq 1.3$ . On the other hand, for  $\Gamma_1 = 1.32$ , the outcomes are completely different from those for other two cases as in the case of  $A = 0.1$ .

Model	$A$	$K_0$	$\Gamma_1$	$\Gamma_2$	$M_*$	$M$	$J/M^2$	$L$	Stability
M5c1C	0.1	5e14	1.28	2.75	1.287	1.288	1.380	144	Unstable
M5c2A	0.1	5e14	1.3	2.5	1.384	1.384	1.103	147	Stable
M5c2C	0.1	5e14	1.28	2.75	1.224	1.235	1.204	147	Unstable
M7b3A	0.25	7e14	1.3	2.5	2.234	2.235	1.154	182	Stable
M7b3C	0.25	7e14	1.28	2.75	1.944	1.946	1.195	182	Stable
M7c2A	0.1	7e14	1.3	2.5	2.347	2.348	1.081	170	Stable
M7c2C	0.1	7e14	1.28	2.75	2.106	2.108	1.172	170	Unstable
M7c3A	0.1	7e14	1.3	2.5	2.263	2.265	0.939	171	Stable
M7c3C	0.1	7e14	1.28	2.75	2.014	2.016	1.024	171	Unstable
M7c4C	0.1	7e14	1.28	2.75	1.956	1.958	0.922	172	Stable

TABLE IV. Parameters and numerical results for three-dimensional simulations.  $K_0$ ,  $M_*(M)$ ,  $\rho_{\max}$ , and  $L$  are listed in units of cgs,  $M_\odot$ ,  $\text{g}/\text{cm}^3$ , and km, respectively. The ADM mass  $M$  is still nearly equal to the baryon rest-mass  $M_*$ . In the last column, the stability against the bar-mode is shown.

### E. Candidates of nonaxisymmetric dynamical instabilities

As reviewed in Sec. I, nonaxisymmetric dynamical instabilities of rotating stars in isolated equilibrium may set in when the value of  $\beta$  becomes larger than  $\sim 0.27$  or when the degree of differential rotation is sufficiently high. It is found that to achieve  $\beta_{\max} \gtrsim 0.27$ , the following conditions are necessary; (i) the progenitor of the collapse should be highly differentially rotating with  $A \lesssim 0.25$ ; (ii) the progenitor has to be moderately rapidly rotating with  $0.01 \lesssim \beta_{\text{init}} \lesssim 0.02$ ; (iii) the progenitor should be massive enough to make a compact core for which an efficient spin-up is possible.

As indicated in [21,28], even in the case of  $\beta < 0.27$ , nonaxisymmetric dynamical instabilities may set in if the degree of differential rotation is sufficiently large. To achieve such a state, the conditions (i) and (ii) are also necessary. In addition, the following condition is required: (iv) the depletion factor of the internal energy and the pressure in an early stage of collapse during which  $\rho \ll \rho_{\text{nuc}}$  is large enough to induce a significant collapse in the central region for making a torus-like structure and a steep profile of rotational angular velocity. In the next section, we present numerical results of the three-dimensional simulations and illustrate that the condition (iv) plays an important role for the onset of nonaxisymmetric dynamical instabilities.

## V. RESULTS IN THREE-DIMENSIONAL SIMULATIONS

### A. Features of nonaxisymmetric dynamical instabilities

As described in Sec. IV, there are several candidate models for which nonaxisymmetric dynamical instabilities may set in. We performed the three-dimensional simulations focusing on the candidates in which  $\beta_{\max} \gtrsim 0.27$  and  $\beta \sim 0.2$  after bounce. In this paper, however, we do not pay attention to the models in which oscillating stars with the period  $\gtrsim 10$  msec are formed since the simulations for such models take too much computational time.

In the simulations, we initially superimposed a nonaxisymmetric bar-mode density perturbation as defined in Eq. (54). Specifically, we picked up models M5c1, M5c2, M7b3, M7c2, M7c3, and M7c4 with  $(\Gamma_1, \Gamma_2) = (1.3, 2.5)$  and  $(1.28, 2.75)$  (referred to them, e.g., as M5c1A and M5c1C) as listed in Table IV. Since the matter in the outer region is discarded in preparing the initial conditions for the three-dimensional simulations according to Eq. (53), the mass and the angular momentum are smaller than those in the corresponding axisymmetric simulations by 10–20%. As a consequence, the numerical results deviate slightly from those obtained by the axisymmetric simulations even in the case that nonaxisymmetric deformation is small. However, qualitative differences between two results are not found and also the quantitative disagreement is small (see below).

In this paper, the dynamical stability against bar-mode deformation is analyzed using a distortion parameter defined by

$$\eta \equiv (\eta_+^2 + \eta_\times^2)^{1/2}, \quad (57)$$

where

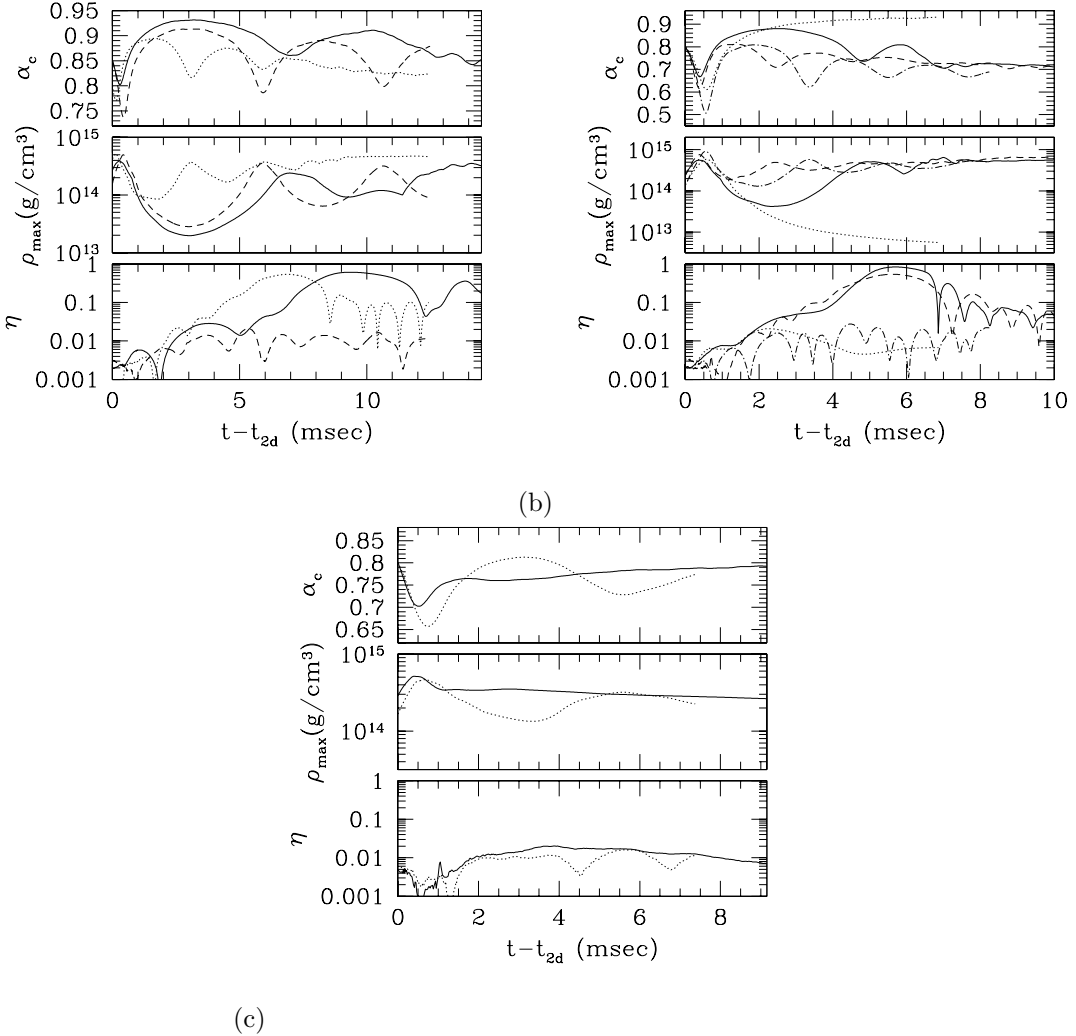


FIG. 9. Evolution of  $\rho_{\max}$ ,  $\alpha_c$ , and  $\eta$  in the three-dimensional simulations (a) for models M5c1C (solid curves), M5c2A (dashed curves), and M5c2C (dotted curves), (b) for models M7c2A (dotted curves), M7c2C (solid curves), M7c3A (dotted-dashed curves), and M7c3C (dashed curves), and (c) for models M7b3A (dotted curves) and M7b3C (solid curves). Here,  $t_{2d}$  denotes the time at which we change to the three-dimensional code;  $t_{2d} = 85.4, 115.1, 85.1, 114.9, 85.1, 121.2, 84.7, 118.6,$  and  $86.7$  msec for M5c1C, M5c2A, M5c2C, M7c2A, M7c2C, M7c3A, M7c3C, M7b3A, and M7b3C, respectively.

$$\eta_+ \equiv \frac{Q_{xx} - Q_{yy}}{Q_{xx} + Q_{yy}}, \quad \eta_\times \equiv \frac{2Q_{xy}}{Q_{xx} + Q_{yy}}, \quad (58)$$

and

$$Q_{ij} = \int_{\rho > \rho_{\text{cut}}} \rho_* x^i x^j d^3x. \quad (59)$$

Here, the integration is carried out only for  $\rho \geq \rho_{\text{cut}}$  where  $\rho_{\text{cut}}$  is a selected cutoff density. In this paper, we chose as  $\rho_{\text{cut}} = \rho_{\max}/100$  to focus on the high-density region. For comparison, we also chose the cutoff density as zero (i.e., the distortion parameter is defined in terms of  $I_{ij}$ ). In this case, the distortion parameter is denoted as  $\eta_0$ . In the following, we primarily adopt  $\eta$ , and if the value of  $\eta$  grows exponentially, we judge that the model is dynamically unstable.

In Fig. 9, we show the evolution of  $\rho_{\max}$ ,  $\alpha_c$ , and  $\eta$  for models M5c1C, M5c2A, M5c2C, M7b3A, M7b3C, M7c2A, M7c2C, M7c3A, and M7c3C. For models M5c2A, M7b3A, M7b3C, M7c2A, M7c3A, and M7c4C,  $\eta$  (and also  $\eta_0$ ) does not increase exponentially (cf. Table IV). This implies that these models are dynamically stable against bar-mode deformation. For models M5c1C, M5c2C, M7c2C, and M7c3C, on the other hand, the values of  $\eta$  approximately

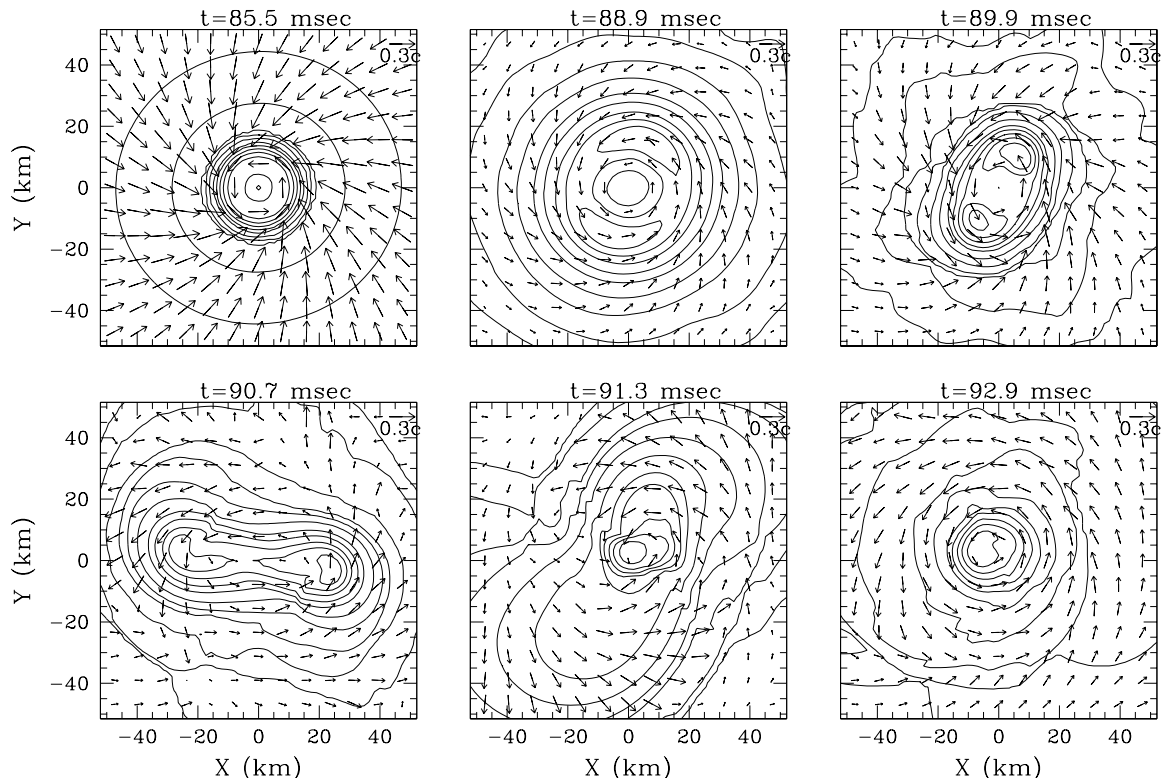


FIG. 10. Snapshots of the density contour curves for  $\rho$  in the equatorial plane for model M7c2C. The solid contour curves are drawn for  $\rho/\rho_{\max} = 1, 0.8, 0.6, 0.4, 0.2$ , and  $10^{-j/2}$  for  $j = 2, \dots, 8$ . Vectors indicate the local velocity field  $(v^x, v^y)$ , and the scale is shown in the upper right-hand corner.

increase in proportional to  $e^{t/\tau}$  where  $\tau$  denotes a characteristic growth time. Thus, these models are unstable. The growth time  $\tau$  of these models is approximately 0.8–1 msec. This is the same order of magnitude as the dynamical time scale  $\rho_c^{-1/2}$ . Thus, the instabilities found here are indeed the dynamical instabilities.

In Figs. 10–12, we display the snapshots of the density contour curves and velocity vectors for the selected time slices for models M7c2C, M7c3C, and M5c2C. In all the models, the collapse proceeds in approximately axisymmetric manner throughout the initial collapse to the first bounce, forming a torus-like structure. For M7c2C, after the first bounce, the formed core expands by a large factor, and then, collapses again. In this second collapse, nonaxisymmetric instabilities grow significantly: In the torus-like high-density region, two density peaks are formed (third panel of Fig. 10). Then, the separation of the density peaks increases, and a bar-like structure is formed (fourth panel), developing spiral arms in the outer region. Subsequently, the separation decreases, and they eventually merge and form a single peak (fifth and sixth panels). In the outer region, spiral arms are developed, which play a role for transferring the angular momentum of the formed core to the outer region. Because of this angular momentum transfer as well as the dynamical friction force to the bar from the surrounding matter, the nonaxisymmetric structure of the central core is quickly erased and the protoneutron star eventually relaxes to a slightly nonaxisymmetric quasistationary state.

For model M7c3C, the nonaxisymmetric instabilities grow in a similar manner to that of M7c2C. In this case, however, the maximum value of  $\eta$ , which denotes the achieved maximum degree of nonaxisymmetric deformation, is slightly smaller. This seems to reflect the fact that the angular momentum is not as large as that of M7c2C. For model M5c2C, the evolution is very similar to that of M7c3C. However, the growth rate of  $\eta$  for M5c2C is slightly smaller than for M7c2C. The reason is that the mass and the compactness of the outcome formed after the collapse are smaller, and hence, the growth time of the nonaxisymmetric dynamical instabilities, which is approximately proportional to the dynamical time scale, becomes longer.

A noteworthy feature for the unstable models is that in the late phase in which the bar-mode perturbation damps, the  $m = 1$  mode grows gradually and becomes a dominate mode eventually. With the growth of this mode, small one-armed spiral arm is formed (see, e.g., the last panels of Figs. 10–12). The excitation of this mode is probably due to the fact that the formed star is highly differentially rotating [55,56]. However, the effect of its growth is not very outstanding since the amplitude of the perturbation is not very large and fairly quickly damps due to the angular

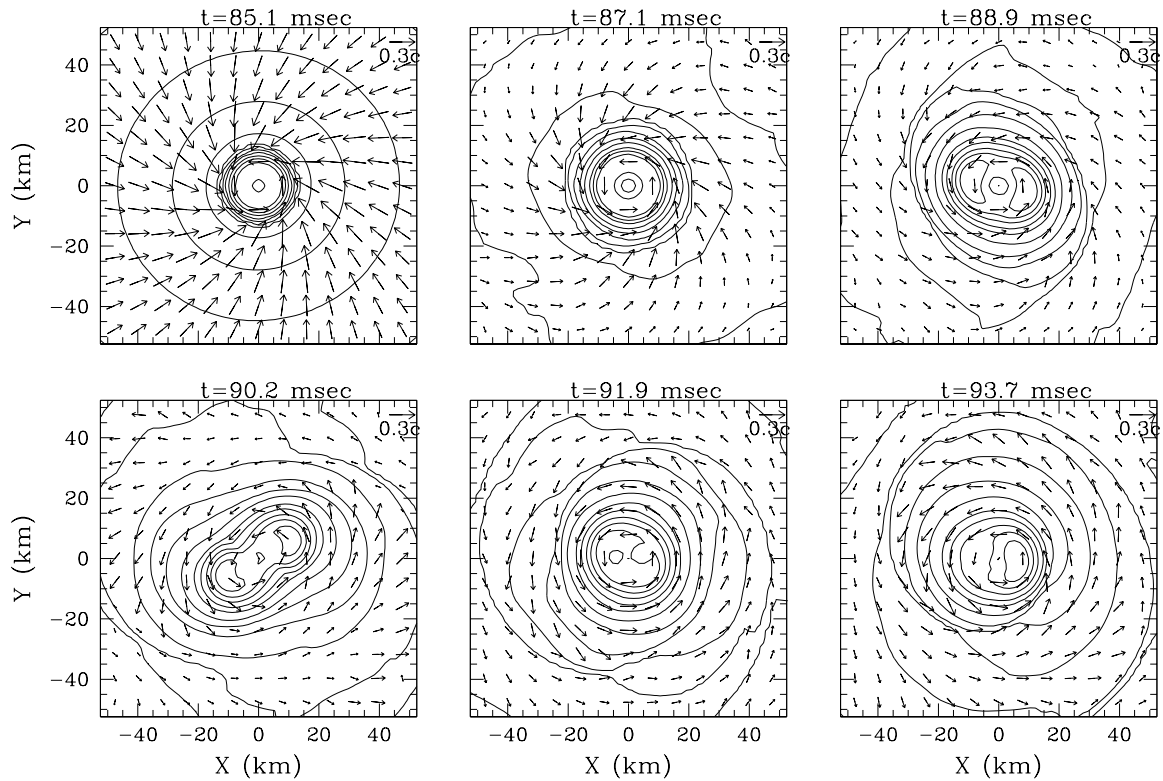


FIG. 11. The same as Fig. 10 but for model M7c3C.

momentum transfer to the outer region. Therefore, we conclude that the onset of  $m = 1$  mode instabilities is not as important as that of the bar-mode for the evolution of the system, although the density configuration of the formed protoneutron star becomes asymmetric due to it.

The formation of the bar and subsequent outward transfer of the angular momentum change the density profile of the protoneutron stars. In Fig. 13, we show the evolution of  $\alpha_c$ ,  $\rho_{\max}$ , and  $\eta$  for models M7c2C and M7c3C in the three-dimensional simulations as well as in the axisymmetric ones. To illustrate that the convergence is approximately achieved, the three-dimensional results with  $N = 156, 188,$  and  $220$  are shown together. In the early stage of the evolution ( $t \lesssim 88$  msec) in which the amplitude of the bar-mode perturbation is small, the results of the three-dimensional and axisymmetric simulations are in good agreement: i.e.,  $\alpha_c$  and  $\rho_{\max}$  are simply in a damped oscillation. Slight disagreement between the results of the three-dimensional and axisymmetric simulations is likely due to the fact that we discard the matter located in the outer region in the three-dimensional simulations. In a stage in which the system is approximately axisymmetric, shock dissipation which damps the oscillation is only the mechanism for modifying the density profile. On the other hand, in the late stage with  $\eta \gtrsim 0.1$  (see Figs. 13 (c) and (d)),  $\rho_{\max}$  ( $\alpha_c$ ) gradually increases (decreases) with time in the three-dimensional simulations. This reflects the effect of the angular momentum transfer by which the centrifugal force in the inner region is weakened and the formed object becomes more compact than the outcome in the axisymmetric simulations. In particular, the effect is remarkable for model M7c2C. In this case, an oscillating (type O-A) star (not a protoneutron star in the definition of this paper) is formed in the early phase of the axisymmetric simulation, while in the three-dimensional simulation, the protoneutron star is promptly formed because of the quick contraction due to the outward transfer of the angular momentum. For more massive cases with  $M \gtrsim 3M_{\odot}$ , protoneutron stars which are supported by strong differential rotation may be formed first [59], but the angular momentum transfer may trigger black hole formation. This effect may also play an important role in stellar collapse of very massive ( $M \gtrsim 250M_{\odot}$ ) stars (population III stars) which is triggered by the electron-positron pair creation instability [60]. Very massive stars are likely to be rapidly rotating [61], and the collapse may not result directly in a black hole but in very massive self-gravitating disks [62]. The disks will be dynamically unstable against nonaxisymmetric deformation and the resulting angular momentum transfer by a nonaxisymmetric structure may induce black hole formation.

Figure 13 also shows that with increasing the value of  $N$ , the numerical results achieve a convergence. The results of  $N = 188$  and  $220$  agree well (except for those in the very late time for which the numerical error is accumulated

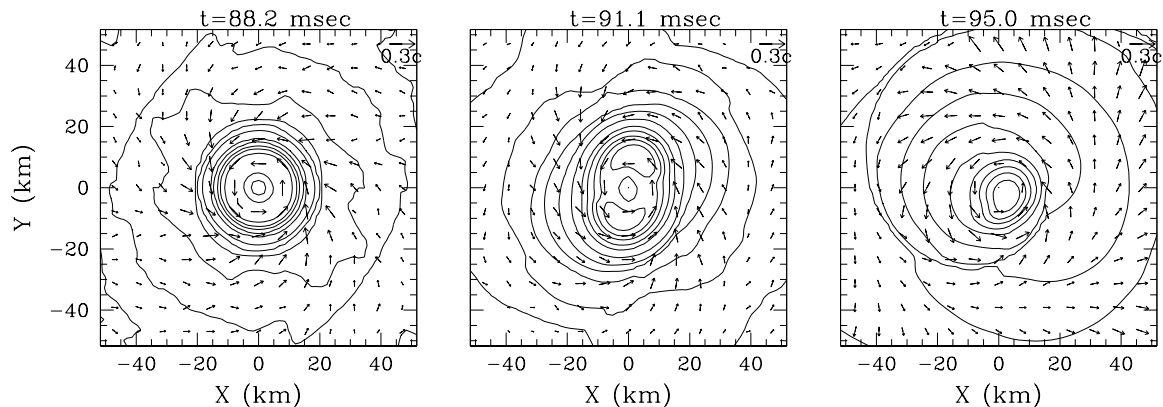


FIG. 12. The same as Fig. 10 but for model M5c2C.

too much), implying that a convergent result is obtained with  $N \sim 200$ . By the way, the period of the quasiradial oscillation becomes spuriously longer due to the larger numerical dissipation with the smaller value of  $N$ . Such spurious effect may lead to underestimation of the growth rate and the achieved maximum value of  $\eta$ . The convergent test carried out here gives us a caution that we have to guarantee a sufficient grid resolution in this problem.

In the lower panels of Fig. 13(c) and (d), we display the evolution of  $\eta_0$  to compare with that of  $\eta$ . For model M7c2C,  $\eta_0$  increases to be much larger than the initial value. However, the value of  $\eta_0$  is smaller than that of  $\eta$  even when the bar-mode grows to a nonlinear regime. This implies that the bar structure is formed mainly in the central region. This feature is more outstanding for model M7c3C in which the increase of  $\eta_0$  from the initial value is not seen. Thus, we conclude that the bar-mode perturbation is amplified only in the central region. This is reasonable since in the models with  $A = 0.1$ , the outcomes are rapidly rotating only in the central region.

### B. Criterion for the onset of nonaxisymmetric dynamical instabilities

Models M7c2C and M7c3C are dynamically unstable against bar-mode and  $m = 1$  mode deformation, while model M7c4C is stable for both modes. This implies that for the onset of dynamical nonaxisymmetric instabilities, high values of  $\beta$  are necessary for given values of  $\Gamma_1$  and  $M$ .

All the models with  $\Gamma_1 = 1.3$  that we picked up here are stable. On the other hand, the models with  $\Gamma_1 = 1.28$  are much more prone to be unstable. This suggests that only for a sufficiently small value of  $\Gamma_1 \lesssim 1.28$ , the collapsing star can be unstable. As mentioned in Sec. IV, for the smaller value of  $\Gamma_1$  (for the larger depletion factor of the internal energy and the pressure at the onset of collapse), the outcomes are more torus-like than those for other values of  $\Gamma_1$ , and also, the degree of differential rotation is larger. These facts are likely reasons that models with  $\Gamma_1 = 1.28$  are more subject to the dynamical instabilities.

Even with  $M \approx 1.5M_\odot$  (models M5c1C and M5c2C), nonaxisymmetric bar-mode instabilities set in, although the maximum values of  $\beta$  and compactness for the outcomes are smaller than for models M7c2C and M7c3C. This indicates that the mass and compactness achieved in the collapse are not very important parameters for triggering the bar-mode instabilities as far as  $M$  is larger than  $\sim 1.5M_\odot$ . However, it should be noted that general relativistic effects certainly help making a compact outcome. Thus, if the mass is much smaller than  $\sim 1.5M_\odot$ , nonaxisymmetric instabilities may not set in.

Although a high value of  $\beta$  is necessary, the onset of the nonaxisymmetric dynamical instabilities is not simply determined by the value of  $\beta$ ; i.e., although a large value of  $\beta \gtrsim 0.27$  is preferable for the onset, it is neither the necessary nor the sufficient conditions. The first evidence for this statement is that the values of  $\eta$  for the unstable models do not increase at the first bounce at which the value of  $\beta$  becomes maximum with  $\beta_{\max} \gtrsim 0.27$ . The growth of the perturbation is significantly induced in the subsequent bounce stages. Also, model M7c2A is dynamically stable although  $\beta_{\max} \approx 0.33$ . These show that even if  $\beta$  exceeds  $\sim 0.27$ , the nonaxisymmetric perturbations do not grow. Probably, the duration of the phase for which  $\beta > 0.27$  would have to be much longer than the dynamical time scale for the onset of the dynamical instabilities.

Second, the value of  $\beta$  during the growth of the bar-mode perturbation is smaller than 0.27 for any unstable model. In Fig. 14, we show the time evolution of  $\beta$  for models M7c2C, M7c3A, M7c3C, and M5c2C. It shows that during the growth of the perturbation,  $\beta$  for models M7c3C and M5c2C is at most  $\sim 0.25$  and in average  $\sim 0.2$ , which is

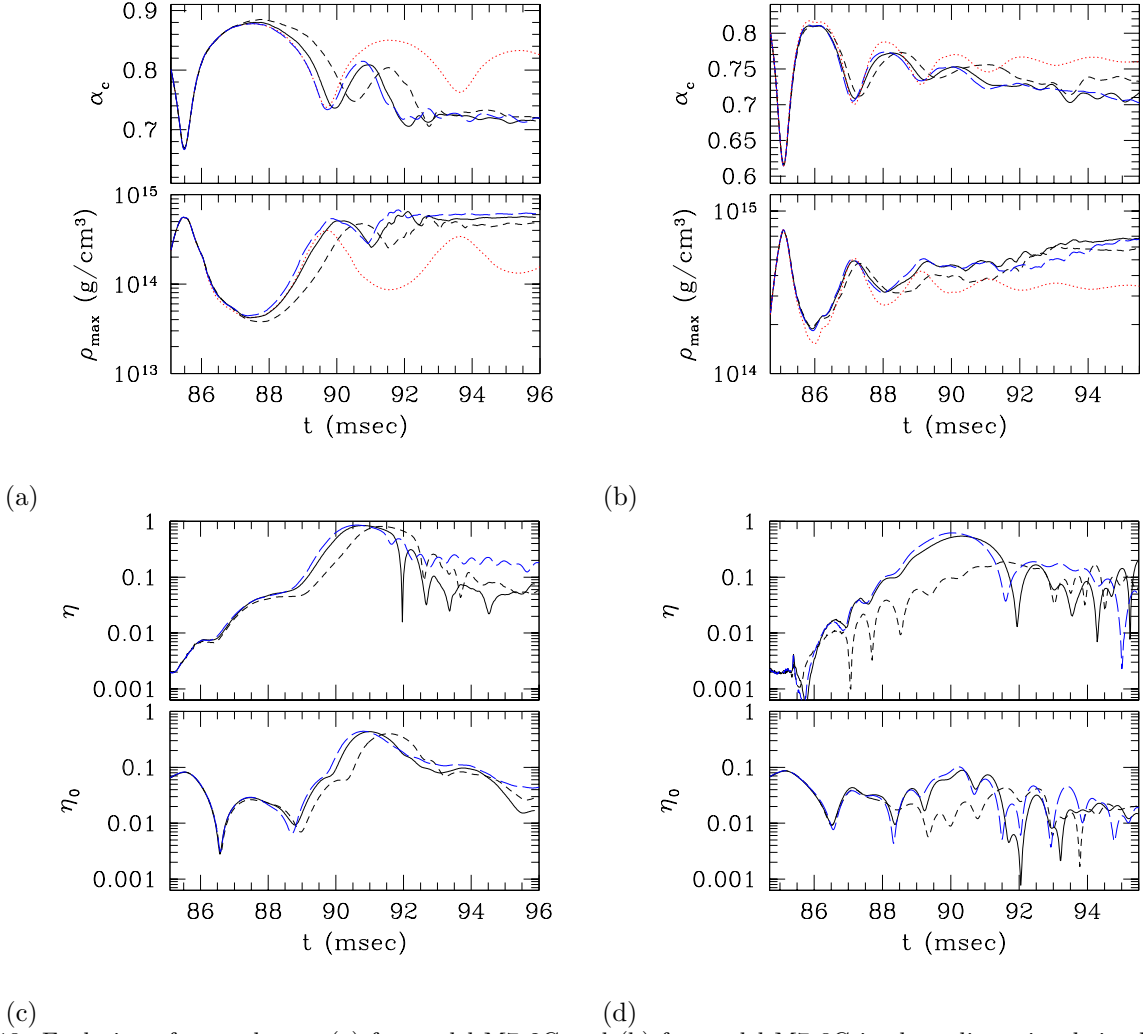


FIG. 13. Evolution of  $\alpha_c$  and  $\rho_{\max}$  (a) for model M7c2C and (b) for model M7c3C in three-dimensional simulations with  $N = 156$  (dashed curves), 188 (solid curves), and 220 (long-dashed curves) as well as in axisymmetric simulation (dotted curves). Evolution of  $\eta$  and  $\eta_0$  (c) for model M7c2C and (d) for model M7c3C in three-dimensional simulations with varying grid resolution.

much smaller than the widely-believed critical value  $\sim 0.27$ . There are at least three possible reasons that  $\beta$  may be smaller than 0.27 for the onset of the nonaxisymmetric dynamical instabilities. The first one is that the effective value of  $\beta$  in the high-density region may be larger than the global value, and may be large enough for the onset of the nonaxisymmetric dynamical instabilities. This is likely to be the case in particular for the highly differentially rotating collapse since the effective value of  $\beta$  in the central high-density region where the nonaxisymmetric perturbation grows dominantly is larger than the whole value for such cases. The second possibility is that the onset of the nonaxisymmetric dynamical instabilities is due to the high degree of differential rotation as indicated in a Newtonian simulation [28]. In this case, the high value of  $\beta > 0.27$  is not necessary. The third possibility is that general relativistic effects reduce the critical value of  $\beta$  below 0.27. Indeed, in [15], we showed that the critical value of  $\beta$  can be decreased by  $\sim 10\%$  due to the general relativistic effects for compact stars with the compactness  $\sim 0.1-0.2$ . All these possibilities show that the critical value of  $\beta$  for the onset of the nonaxisymmetric dynamical instabilities may be smaller than 0.27 depending sensitively on several parameters, and thus, it cannot be uniquely determined.

Figure 14 also shows that the values of  $\beta$  for models M7c3A and M7c3C are not very different during the oscillation phase although they are stable and unstable against bar-mode deformation, respectively. This also illustrates that the value of  $\beta$  does not uniquely determine the dynamical stability. As shown in Fig. 7, on the other hand, the profiles of the density and the rotational angular velocity in the central region are different between two models. Thus, in this case, the degree of differential rotation and the steepness of the density profile play an important role for determining

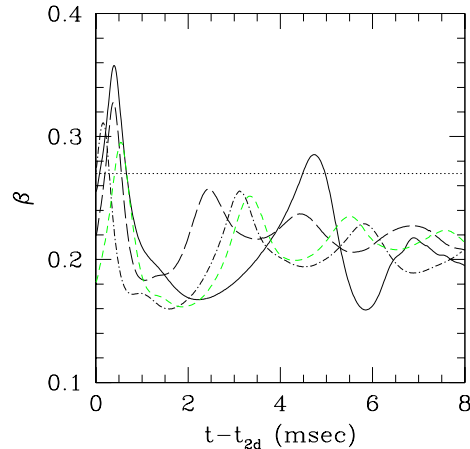


FIG. 14. Evolution of  $\beta$  for models M7c2C (solid curve), M7c3C (long-dashed curve), M7c3A (dashed curve), and M5c2C (dotted-dashed curves) in three-dimensional simulations. The values of  $t_{2d}$  are listed in the caption of Fig. 9. The dotted line denotes  $\beta = 0.27$ .

the stability.

The case with  $\Gamma_1 = 1.28$ , in which the depletion of the pressure and the internal energy in an early stage of collapse with  $\rho \ll \rho_{\text{nuc}}$  is largest among the three cases, is more subject to the nonaxisymmetric dynamical instabilities. This indicates that a large depletion of the internal energy and the pressure in the early stage is an essential element for the onset of the nonaxisymmetric dynamical instabilities. The reason is that for the larger depletion factor, the collapse in the central region proceeds significantly to make a compact core, and hence, to increase the spin of the central region as illustrated in the axisymmetric simulations (cf. Fig. 7). In a realistic phenomena, the depletion of the pressure and the internal energy in the early stage is determined by the partial photo-dissociation of the iron to lighter elements, by the electron capture, and by the neutronization [48,49]. Since the depletion factor is a crucial parameter, an appropriate modeling for such microphysical processes will be necessary for a more detailed study on the nonaxisymmetric dynamical instabilities in the future.

No evidence for fragmentation of protoneutron stars is found in the first  $\sim 10$ – $20$  msec after the bounce in the present numerical simulations. Previous studies in the field of protostar formation from collapsing gas clouds (e.g., [63]) show that the fragmentation occurs when the thermal energy at an initial stage of the collapse is much smaller than the gravitational potential energy: In the case of the small thermal energy, a torus-like or a disk-like structure is formed as a result of the collapse and subsequently the fragmentation takes place. This indicates that if the value of  $\Gamma_1$  is much smaller than 1.28 (i.e., if the fraction of the depletion of the internal energy and the pressure in an early stage of collapse is much larger than 16%), the fragmentation may occur during the stellar core collapse. However, such an extremely small value of  $\Gamma_1$  (an extremely large value of the depletion factor) is unlikely to be achieved in the stellar core collapse [48,49], and therefore, we infer that the fragmentation of protoneutron stars would not occur in nature, at least in a few 10 msec after the stellar collapse.

To summarize, the nonaxisymmetric dynamical instabilities set in only for the case that the following conditions are satisfied: (i) the progenitor of the stellar core collapse is rapidly rotating with the initial value of  $\beta \gtrsim 0.01$ , (ii) the degree of differential rotation for the velocity profile of the initial condition is very high with  $A \lesssim 0.1$ , (iii) the depletion factor of the pressure and the internal energy in an early stage of collapse in which  $\rho \ll \rho_{\text{nuc}}$  should be large enough to induce a rapid collapse in the central region of the stellar core and for an efficient spin-up. With the increase of stellar core mass, the maximum value of  $\beta$  achieved during the collapse is increased, but this does not significantly change the stability property as far as  $M$  is larger than  $\sim 1.5M_{\odot}$ . It is also found that the value of  $\beta$  does not uniquely determine the property of the dynamical stabilities.

### C. Gravitational waveforms from nonaxisymmetrically deformed stars

In Fig. 15, we show gravitational waveforms and total emitted energy and angular momentum as a function of retarded time for models M7c2C, M7c3C, and M5c2C. For these models, nonaxisymmetric dynamical instabilities set in after the bounce resulting in formation of a bar and spiral arms and in excitation of gravitational waves with  $m = 2$

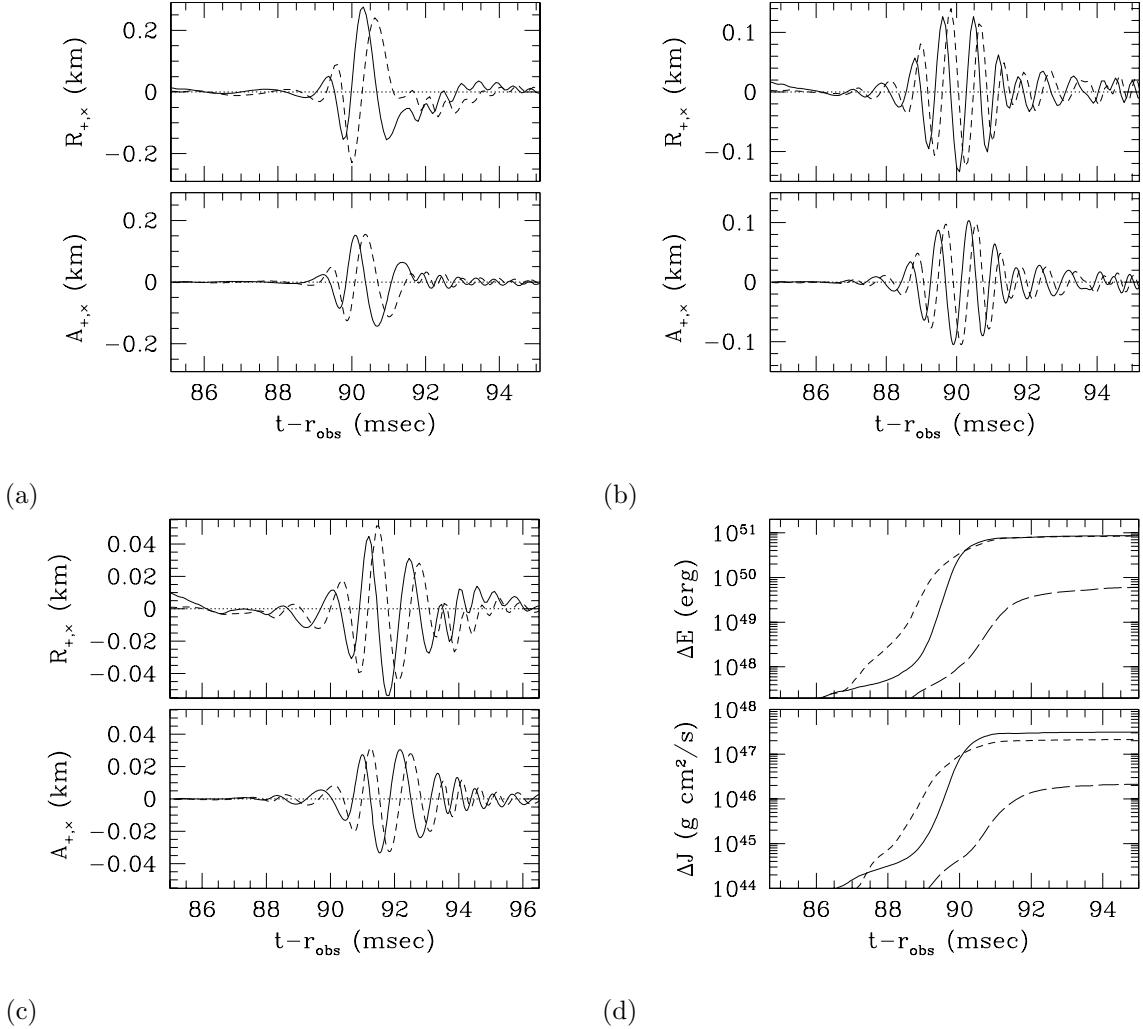


FIG. 15. Gravitational waveforms in the gauge-invariant wave extraction method ( $R_{+,x}$ ) and in the quadrupole formula ( $A_{+,x}$ ) (a) for M7c2C, (b) for M7c3C, and (c) for M5c2C. (d) Total emitted energy and angular momentum as a function of retarded time for models M7c2C (solid curves), M7c3C (dashed curves), and M5c2C (long-dashed curves).

modes. Gravitational waveforms are computed both by the gauge-invariant wave extraction and by the quadrupole formula.

Figures show that with the amplification of  $\eta$ , the amplitude of gravitational waves are increased. However, once it reaches the maximum, the amplitude damps quickly as in the evolution of  $\eta$ . This is due to the effect that the bar-mode perturbation plays a role for transferring the angular momentum from the inner region to the outer one. Eventually, the bar-mode perturbation damps, resulting in a quick damping of gravitational wave amplitude. The damping is in particular outstanding for model M7c2C. This is due to the fact in this model, the amplitude of the bar-mode is largest, and hence, the angular momentum transfer is most effective. Due to this fact, the total emitted energy for models M7c2C and M7c3C becomes approximately identical although the maximum amplitude of gravitational waves for M7c2C is about twice larger.

In isolated rotating stars, once the bar-mode instabilities set in and saturate, the amplitude of their perturbation remains approximately constant, resulting in emission of quasiperiodic gravitational waves in a dissipation time scale of gravitational radiation which is much longer than the dynamical time scale (e.g., [28]). However, in the rotating core collapse, the amplitude of gravitational waves is damped by the angular momentum transfer from the bar to the surrounding matter, for which the time scale is nearly equal to the dynamical time scale and much shorter than the emission time scale of gravitational radiation.

The maximum amplitude of gravitational waves for model M7c2C is by a factor of  $\sim 2$  larger than that for M7c3C, reflecting that the degree of nonaxisymmetric deformation is larger. The amplitude for model M5c2C is by a factor

of  $\sim 2.5$  smaller than that of M7c3C, although the initial value of  $\beta$  is approximately identical and the waveforms are very similar for these two models. According to the quadrupole formula, the amplitude of gravitational waves is approximately proportional to  $M^2$  if the radius of the formed protoneutron star is identical. Thus, the dependence on mass is reflected in the amplitude.

In the evolution of models M7c2C, M7c3C, and M5c2C, the  $m = 1$  mode perturbation grows in the late phase of the evolution. However, this does not affect the amplitude of gravitational waves significantly, since the amplitude of the perturbation is not very large and the  $m = 1$  mode does not contribute to the lowest-order (mass quadrupole) waveforms in the three-space of the reflection symmetry with respect to the equatorial plane.

For models M7c2C and M7c3C, the maximum values of  $R_{+,x}$  are  $\sim 0.25$  km and  $0.15$  km, respectively. For M5c2C, it is even smaller  $\sim 0.05$  km. The amplitude of gravitational waves,  $h$ , observed at a distance of  $r$  along the optimistic direction ( $\theta = 0$ ) is written as

$$h \approx 10^{-21} \left( \frac{R_{+,x}}{0.31 \text{ km}} \right) \left( \frac{10 \text{ Mpc}}{r} \right). \quad (60)$$

This implies that the observed amplitude at a distance of 10 Mpc is at most  $h \lesssim 8 \times 10^{-22}$  for initial core mass  $M \sim 2.5M_\odot$  and  $h \sim 1.5 \times 10^{-22}$  for  $M \sim 1.5M_\odot$ .

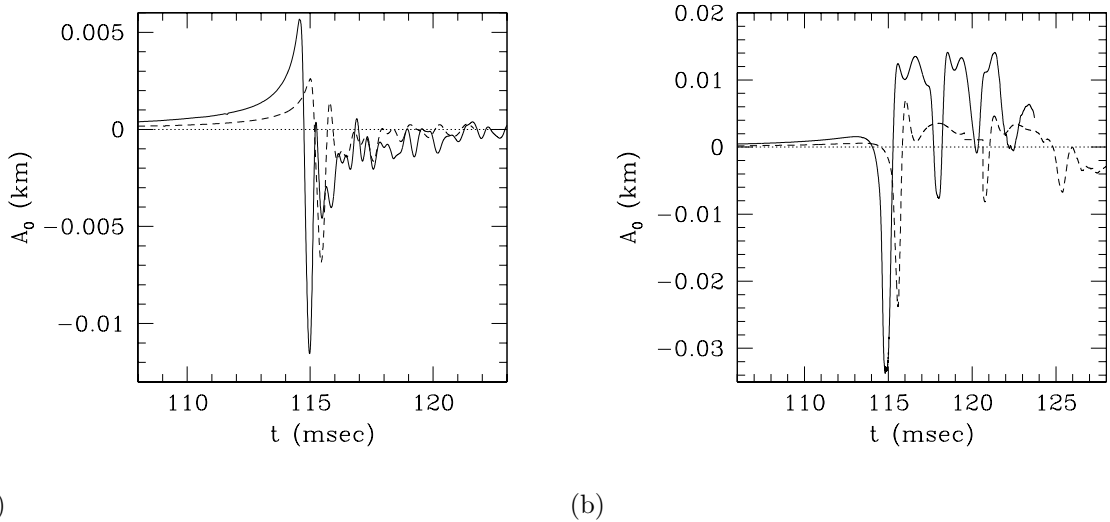
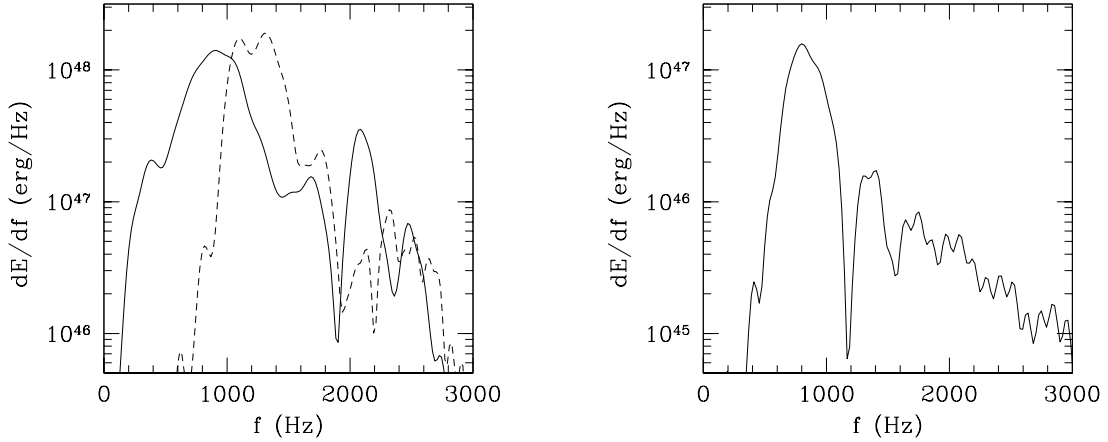


FIG. 16.  $A_0$  in the axisymmetric simulations (a) for models M7a1 (solid curves) and M5a1 (dashed curves), and (b) for models M7c3 (solid curve) and M5c2 (dashed curve) with  $\Gamma_1 = 1.3$  and  $\Gamma_2 = 2.5$ .

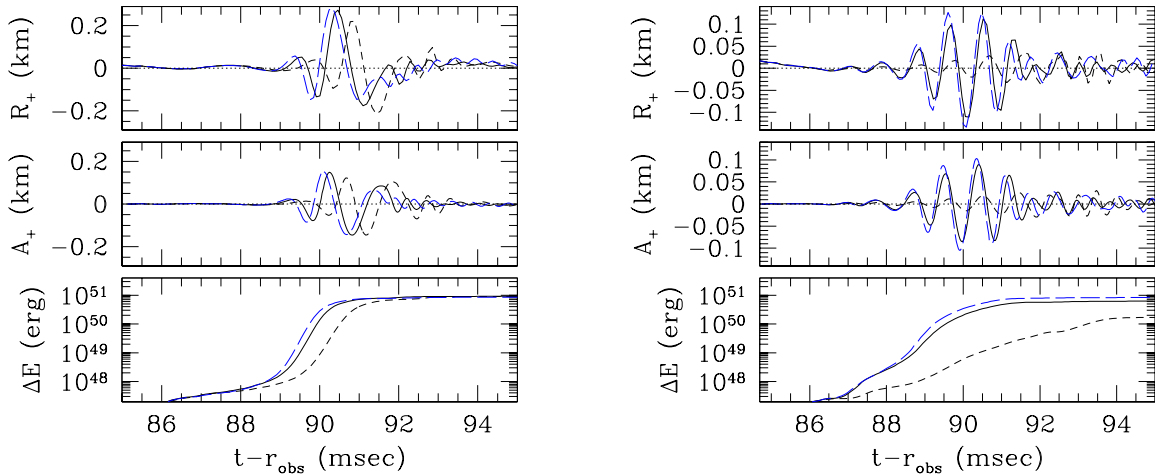
To compare the amplitude of gravitational waves from the bar-mode deformation with that from axisymmetric collapse, we show  $A_0$  for models M5a1, M7a1, M5c2, and M7c3 with  $\Gamma_1 = 1.3$  and  $\Gamma_2 = 2.5$  in the axisymmetric simulations in Fig. 16. As mentioned in [12], it is difficult to extract gravitational waves of small amplitude from the metric in the axisymmetric simulations, and hence, only the waveforms by the quadrupole formula are presented here. Although it provides only an approximate waveform, the wave phase can be accurately computed and the error of the amplitude will be at most  $\sim 10\%$ . Figure 16 indicates that for the initial mass  $M \sim 2.5M_\odot$ , the maximum amplitude is at most 0.01 km for the rigidly rotating case and 0.02–0.03 km for differentially rotating cases. The values are by a factor of  $\sim 2$  smaller for  $M \sim 1.5M_\odot$ . Thus, the amplitude of gravitational waves of the  $l = m = 2$  modes from the nonaxisymmetric dynamical instabilities is  $\sim 10$  times as large as that in the axisymmetric case. On the other hand, those amplitudes are not as large as the maximum amplitude of gravitational waves from of coalescing binary neutron stars in close circular orbits [36]. Thus, the nonaxisymmetric deformation in the stellar core collapse is not as a stronger emitter as coalescing binary neutron stars.

For model M7c2C (M7c3C), the total emitted energy and angular momentum are about  $9 \times 10^{50}$  erg ( $9 \times 10^{50}$  erg) and  $3 \times 10^{47}$  g cm<sup>2</sup>/sec ( $2 \times 10^{47}$  g cm<sup>2</sup>/sec), respectively. These values are about 0.03% (0.03%) of the total mass energy ( $M_*c^2$ ) and 0.7% (0.6%) of the total angular momentum, respectively, and are much larger than those in the axisymmetric collapse (e.g., [10]). However, they are not as large as those in merger of binary compact objects in which  $\gtrsim 1\%$  of the total mass energy and  $\gtrsim 10\%$  of the angular momentum are dissipated by gravitational waves in the final phase of the merger [36]. Thus, in the stellar collapse, the radiation reaction by gravitational waves are not likely to play an important role for the dynamics of bounce and oscillation of the protoneutron star. For model

M5c2C, these values are much smaller because of its small mass and small compactness achieved. Hence, the effect of gravitational wave emission is less important.



(a) (b)  
 FIG. 17. Energy power spectra of  $l = m = 2$  modes (a) for models M7c2C (solid curve) and M7c3C (dashed curve), and (b) for M5c2C.



(a) (b)  
 FIG. 18. Gravitational waveforms and energy luminosity (a) for model M7c2C and (b) for model M7c3C with  $N = 156, 188,$  and  $220$ . The long-dashed, solid, and dashed curves denote the results with  $N = 220, 188,$  and  $156$ .

Comparison of gravitational waveforms computed by the gauge-invariant wave extraction method and by the quadrupole formula shows that the wave phase in the two results agree approximately (besides a systematic phase shift). However, the amplitude disagrees by a factor of  $\lesssim 2$ . As pointed out in [12], in the quadrupole formula, the amplitude is underestimated by a factor of  $M/R \sim 0.1\text{--}0.2$  where  $R$  here denotes the characteristic radius of the outcome after the collapse. On the other hand, the amplitude in the gauge-invariant wave extraction method is likely to be overestimated because the waveforms are extracted in a local wave zone [44]: In this paper,  $L \sim \lambda/2 < \lambda$  where  $\lambda$  is the wavelength of gravitational waves  $\sim 300$  km, and thus, the amplitude would be overestimated by a factor of 10–20% [44]. Hence, the true amplitude would be between two results. However, besides the disagreement in the amplitude, two methods provide qualitatively the identical results. This reconfirms that the quadrupole formula is a reasonable method for approximately computing gravitational waveforms even in fully general relativistic simulations, in the absence of black holes.

In Fig. 17, we show the energy power spectrum of  $m = 2$  modes (a) for models M7c2C (solid curve) and M7c3C (dashed curve) and (b) for model M5c2C. The Fourier spectrum is computed from gravitational waveforms in terms of the gauge-invariant wave extraction. The spectrum for model M7c2C is broader in a low frequency region with  $f < 1$  kHz than those for other models. This reflects the long oscillation period of this model. The peak frequency is about 0.8–1.3 kHz in these models. These frequencies are determined by the quadrupole f mode frequency of the deformed star formed after the bounce. Namely, the higher peak frequency implies that the outcome is more compact in proportional to  $\sqrt{M/R^3}$ . According to a perturbative study for the quadrupole f mode [64], the frequency of neutron stars becomes  $\sim 2.5\text{--}4$  kHz. The frequency of the oscillation of unstable protoneutron stars is much lower than that of neutron stars. The reason is that the radius of the protoneutron star is larger. Nevertheless, the peak frequency is higher than the best sensitive frequency (between  $\sim 100$  and several 100 Hz) of kilometer size laser-interferometers such as LIGO [34]. As shown in Eq. (60), the amplitude of gravitational waves is not very high if we assume the distance to the source  $\gtrsim 10$  Mpc. Thus, gravitational waves from nonaxisymmetrically deformed protoneutron stars may be promising sources for such gravitational wave detectors only when the stellar collapse happens for  $r \ll 10$  Mpc. On the other hand, the frequency may be in a good range for resonant-mass detectors and/or specially designed advanced interferometers such as the advanced LIGO [34].

To summarize this section, we have found that the amplitude of gravitational waves from dynamically unstable protoneutron stars against nonaxisymmetric deformation is  $\sim 10$  times as large as that from the axisymmetric collapse. However, even in the case that the degree of the nonaxisymmetric deformation is as large as in model M7c2C, the maximum amplitude is  $\lesssim 20\text{--}30\%$  of that in merger of binary neutron stars (e.g., [36]). Since the peak frequency of gravitational waves is fairly high  $\sim 1$  kHz, gravitational waves from nonaxisymmetric dynamical deformation of protoneutron stars may become promising sources for the laser-interferometric gravitational wave detectors only in the case that the event rate for the nonaxisymmetric deformation in the stellar core collapse is large.

Before closing this section, we demonstrate that the convergence with improvement of the grid resolution is achieved fairly well for gravitational waveforms. In Fig. 18, we show the numerical results for models M7c2C and M7c3C with  $N = 156, 188,$  and  $220$ . For the lower grid resolution, the period of the quasiradial oscillation becomes longer. As a result, the growth rate of  $\eta$  becomes smaller. This causes an error in phase of gravitational waves. Also, the lower grid resolution results in underestimating the maximum value of  $\eta$ . As a result, the amplitude of gravitational waves is underestimated. However, with  $N \gtrsim 200$ , the numerical results appear to converge well. Thus, we conclude that with our choice of the grid resolution, a good convergent result is obtained.

## VI. SUMMARY AND DISCUSSION

We have presented the first numerical results of three-dimensional hydrodynamic simulations for stellar core collapse in full general relativity focusing mainly on the criterion for the onset of the bar-mode dynamical instabilities. The nonaxisymmetric dynamical instabilities have been widely studied for isolated rotating stars in equilibrium to this time not only in Newtonian gravity but also in general relativity. However, for nonaxisymmetric dynamical instabilities in rotating stellar core collapse, very little study has been done even in Newtonian gravity [7]. Taking into account such status, we performed the simulations for a wide variety of equations of state, stellar masses, and velocity profiles to clarify the criterion for the onset of the nonaxisymmetric dynamical instabilities as well as the outcomes after their onset.

A number of previous works for isolated rotating stars in equilibrium have clarified that the bar-mode dynamical instabilities can set in when the value of  $\beta$  exceeds  $\sim 0.27$  or when the degree of differential rotation is sufficiently high. Thus, first, we performed axisymmetric simulations of rotating stellar collapse to clarify the conditions that the value of  $\beta$  is amplified beyond  $\sim 0.27$  and that the degree of differential rotation for the outcomes of the collapse becomes very large. We have found the following conditions are necessary to achieve a state with  $\beta_{\max} > 0.27$ : (A) the initial state of the collapse is highly differentially rotating with  $A \lesssim 0.1$ ; (B) the progenitor is moderately rapidly rotating with  $0.01 \lesssim \beta_{\text{init}} \lesssim 0.02$ , but has to be not very rapidly rotating such as  $\beta_{\text{init}} \gtrsim 0.02$ ; (C) the progenitor star is massive enough to achieve a compact state for which a significant spin-up is achieved. However, at the same time, the mass should not be very high to avoid black hole formation. We also found that to achieve a high degree of differential rotation after the collapse, the depletion factor of the pressure and the internal energy in an early stage of collapse in which  $\rho \ll \rho_{\text{nuc}}$  should be large enough to induce a rapid collapse in the central region of the stellar core and resulting efficient spin-up.

Next, to clarify the condition for the onset of nonaxisymmetric dynamical instabilities, we performed three-dimensional simulations. Based on the results of axisymmetric simulations, we picked up models which are likely to become unstable during the collapse and bounce. From the three-dimensional simulations, it is found that the nonaxisymmetric dynamical instabilities set in only for a restricted parameter range as indicated by axisymmetric

simulations. Specifically, the following conditions are required to be satisfied: (i) the progenitor of the stellar core collapse is rapidly rotating with  $0.01 \lesssim \beta_{\text{init}} \lesssim 0.02$ , (ii) the degree of differential rotation for the velocity profile of the initial condition is very high with  $A \lesssim 0.1$ , and (iii) the depletion factor of the pressure and internal energy in the early stage of collapse is large enough to induce a rapid collapse in the central region of the stellar core. Although stellar cores of larger mass have more advantage to form a compact protoneutron star, the stability property depends weakly on the mass as far as  $M \gtrsim 1.5M_{\odot}$ .

Gravitational waves are computed in the case that the bar-mode dynamical instabilities set in. For the case that the bar-mode perturbation grows, the amplitude of gravitational waves increases exponentially, and as a result, burst-type waves are emitted. However, since the bar-mode of the core subsequently damps due to the outward angular momentum transfer in a short time scale  $\sim 2\text{--}3$  msec, the amplitude of gravitational waves decreases quickly. Thus, quasiperiodic gravitational waves, in which the amplitude can be accumulated effectively, are not emitted efficiently after the damping of the nonaxisymmetric perturbation. The maximum amplitude of gravitational waves at a distance of 10 Mpc is  $\sim 4\text{--}8 \times 10^{-22}$  with the frequency  $\sim 1$  kHz for very massive core collapse with initial core mass  $M \sim 2.5M_{\odot}$ . The maximum amplitude is approximately proportional to  $M^2$  for a given value of  $\beta_{\text{init}}$ . For  $M \sim 1.5M_{\odot}$ , thus, the maximum amplitude is  $\sim 1\text{--}2 \times 10^{-22}$  at a distance of 10 Mpc. This amplitude is about 10 times as large as that in the axisymmetric collapse, but  $\sim 20\text{--}30\%$  of the maximum amplitude in the merger of binary neutron stars (e.g., [36]). Thus, the feature of gravitational waves is summarized as follows: (i) burst-type (not quasiperiodic) waves are emitted, (ii) the frequency is relatively high with  $\sim 1$  kHz, and (iii) the amplitude is about 10 times as large as that from axisymmetric collapse, but not as large as that for merge of binary compact objects. These facts imply that only when nonaxisymmetric dynamical instabilities set in for a large fraction of the stellar core collapse, gravitational waves induced by nonaxisymmetric dynamical instabilities of protoneutron stars may become promising sources for kilometer size laser-interferometers.

Besides the dynamical instabilities, there is another route for nonaxisymmetric deformation: *secular instabilities*. As found from Figs. 1 and 6, the value of  $\beta$  in the protoneutron stars formed after the collapse is often larger than the critical value for the onset of secular instabilities  $\sim 0.14$ . According to previous works [65–67], isolated rotating stars of  $\beta \gtrsim 0.14$  can form an ellipsoidal structure due to gravitational radiation, which may become a strong emitter of quasiperiodic gravitational waves with the frequency between 10 and several 100 Hz. However, these studies were performed for isolated stars. In the case of stellar core collapse, the formed protoneutron stars will be surrounded by massive outer envelopes, and thus, the bar-mode perturbation excited by the secular instabilities may be damped quickly due to the angular momentum transfer from the ellipsoidal protoneutron star to the outer envelope as in the case of the dynamical instabilities. A simulation with massive envelope will be necessary to clarify whether the secular instabilities can grow or not. On the other hand, in contrast to the dynamical instabilities, the growth time scale of the secular instabilities is fairly long  $\gtrsim 100$  msec. In such a long time scale, the surrounding matter may be ejected outward or accreted onto the central neutron star in reality, and hence, the secular instabilities may grow as in the isolated stars. However, in such a long time scale, viscous or magnetic dissipation may also play an important role [59] for preventing the growth of the nonaxisymmetric perturbation. At present, it is totally unclear whether the secular instabilities set in or not.

As reported in this paper, the criterion for the onset of nonaxisymmetric dynamical instabilities may depend sensitively on the equations of state for subnuclear density, since with the smaller pressure for  $\rho < \rho_{\text{nuc}}$ , the collapse is accelerated more for an efficient spin-up of the central region. In the present work, we adopted a parametric equation of state for simplicity. To clarify the criterion for the onset of nonaxisymmetric dynamical instabilities more strictly, however, sophisticated equations of state should be adopted. In realistic equations of state, the increase rate of the pressure as a function of the density (i.e., an adiabatic index) significantly decreases at density  $\sim 10^{12}\text{g/cm}^3$  (e.g., [68,69]). This suggests that in a realistic equation of state, collapse of the central region is likely to be accelerated significantly before reaching the nuclear density and, hence, the collapsed core may be more subject to nonaxisymmetric dynamical instabilities. This fact suggests that a simulation with more realistic equations of state is an interesting subject for the future.

Finally, we note the following issue. This paper focuses only on nonaxisymmetric dynamical instabilities of protoneutron stars in the first 10–20 msec after the bounce. The formed protoneutron stars subsequently emit neutrinos and dissipate the thermal energy [49,70]. As a result, they contract gradually in a time scale of  $\sim 10$  sec. Because the angular momentum is conserved approximately, the spin of the protoneutron stars will be increased with the contraction and  $\beta$  may be increased beyond  $\sim 0.27$ . Thus, even in the case that they are stable in the first 10–20 msec after the bounce, they may eventually become unstable after the neutrino cooling. This issue is not investigated in this paper and remains for the future.

### Acknowledgments

We thank Takashi Nakamura for helpful comments. Numerical computations were carried out on the FACOM VPP5000 machine in the data processing center of National Astronomical Observatory of Japan and on the NEC

SX6 machine in the data processing center of ISAS in JAXA. This work is in part supported by Japanese Monbu-Kagakusho Grant (Nos. 15037204, 15740142, and 16029202). YS is supported by JSPS Research Fellowship for Young Scientists (No. 1611308).

---

- [1] E. Müller, *Astron. Astrophys.* **114**, 53 (1982).
- [2] L. S. Finn and C. R. Evans, *Astrophys. J.* **351**, 588 (1990).
- [3] R. Mönchmeyer, G. Schäfer, E. Müller, and R. Kates, *Astron. Astrophys.* **246**, 417 (1991); E. Müller and H.-T. Janka, *Astron. Astrophys.* **103**, 358 (1997).
- [4] S. Bonazzola and J.-A. Marck, *Astron. Astrophys.* **267**, 623 (1993).
- [5] S. Yamada and K. Sato, *Astrophys. J.* **434**, 268 (1994); **450**, 245 (1995); K. Kotake, S. Yamada, and K. Sato, *Phys. Rev. D* **68**, 044023 (2003).
- [6] T. Zwerger and E. Müller, *Astron. Astrophys.* **320**, 209 (1997).
- [7] M. Rampp, E. Müller, and M. Ruffert, *Astron. Astrophys.* **332**, 969 (1998).
- [8] C. Fryer and A. Heger, *Astrophys. J.* **541**, 1033 (2000); C. Fryer, D. E. Holz, and A. Heger, *Astrophys. J.* **565**, 430 (2002).
- [9] C. D. Ott, A. Burrows, E. Livne, and R. Walder, *Astrophys. J.* **600**, 834 (2004).
- [10] H. Dimmelmeier, J. A. Font, and E. Müller, *Astro. Astrophys.* **388**, 917 (2002); **393**, 523 (2002).
- [11] F. Siebel, J. A. Font, E. Müller, and P. Papadopoulos, *Phys. Rev. D* **67**, 124018 (2003).
- [12] M. Shibata and Y. Sekiguchi, *Phys. Rev. D* **69**, 084024 (2004).
- [13] M. Shibata, *Phys. Rev. D* **60**, 104052 (1999).
- [14] M. Shibata, T. W. Baumgarte, and S. L. Shapiro, *Phys. Rev. D* **61**, 044012 (2000).
- [15] M. Shibata, T. W. Baumgarte, and S. L. Shapiro, *Astrophys. J.* **542**, 453 (2000).
- [16] M. D. Duez, S. L. Shapiro, and H.-J. Yo, *Phys. Rev. D* **69**, 104016 (2004).
- [17] L. Baiotti, I. Hawke, P. J. Montero, F. Löffler, L. Rezzolla, N. Stergioulas, J. A. Font, and E. Seidel, gr-qc/0403029.
- [18] J. E. Tohline, R. H. Durisen, and M. McCollough, *Astrophys. J.* **298**, 220 (1985).
- [19] R. H. Durisen, R. A. Gingold, J. E. Tohline, and A. P. Boss, *Astrophys. J.* **305**, 281 (1986).
- [20] H. A. Williams and J. E. Tohline, *Astrophys. J.* **315**, 594 (1987); **334**, 449 (1988).
- [21] J. E. Tohline and I. Hachisu, *Astrophys. J.* **361**, 394 (1990).
- [22] J. L. Houser and J. M. Centrella, *Phys. Rev. D* **54**, 7278 (1996); J. L. Houser, J. M. Centrella, and S. C. Smith, *Phys. Rev. Lett.* **72**, 1314 (1994); S. Smith, J. L. Houser, and J. M. Centrella, *Astrophys. J.* **458**, 236 (1995).
- [23] B. K. Pickett, R. H. Durisen, and G. A. Davis, *Astrophys. J.* **458**, 714 (1996).
- [24] J. Toman, J. N. Imamura, B. K. Pickett, and R. H. Durisen, *Astrophys. J.* **497**, 370 (1998); J. N. Imamura, R. H. Durisen, and B. K. Pickett, *ibid.*, **528**, 946 (2000).
- [25] K. C. B. New, J. M. Centrella, and J. E. Tohline, *Phys. Rev. D* **62**, 064019 (2000).
- [26] J. D. Brown, *Phys. Rev. D* **62**, 084024 (2000).
- [27] Y. T. Liu and L. Lindblom, *Mon. Not. R. astr. Soc.* **342**, 1063 (2001); Y. T. Liu, *Phys. Rev. D* **65**, 124003 (2002).
- [28] M. Shibata, S. Karino, and Y. Eriguchi, *Mon. Not. R. astr. Soc.* **334**, L27 (2002); *ibid.*, **343**, 619 (2003).
- [29] M. Saijo, M. Shibata, T. W. Baumgarte, and S. L. Shapiro, *Astrophys. J.* **548**, 919 (2000).
- [30] J. H. Taylor and J. M. Weisberg, *Astrophys. J.* **345**, 434 (1989).
- [31] H. Umeda, private communication.
- [32] S. E. Woosley, A. Heger, and T. A. Weaver, *Rev. Mod. Phys.* **74**, 1015 (2002).
- [33] J. J. Eldridge and C. A. Tout, *Mon. Not. R. astron. Soc.* **353**, 87 (2004).
- [34] C. Cutler and K. S. Thorne, in *Proceedings of the 16th International Conference on General Relativity and Gravitation*, edited by N. T. Bishop and S. D. Maharaj (World Scientific, 2002), p.72.
- [35] M. Shibata, *Phys. Rev. D* **67**, 024033 (2003).
- [36] M. Shibata, K. Taniguchi, and K. Uryū, *Phys. Rev. D* **68**, 084020 (2003).
- [37] J. A. Font, *Living Review Relativity* **6**, 4, 2000 <http://www.livingreviews.org/Articles/lrr-2003-4/>; F. Banyuls, J. A. Font, J.-Ma. Ibáñez, J. M. Martí, and J. A. Miralles, *Astrophys. J.* **476**, 221 (1997).
- [38] A. Heger, N. Langer, and S. E. Woosley, *Astrophys. J.* **528**, 368 (2000).
- [39] J. L. Friedman, J. R. Ipser, and L. Parker, *Astrophys. J.* **304**, 115 (1986); G. B. Cook, S. L. Shapiro, and S. A. Teukolsky, *Astrophys. J.* **398**, 203 (1992).
- [40] M. Shibata and T. Nakamura, *Phys. Rev. D* **52**, 5428 (1995); See also T. Nakamura, K. Oohara, and Y. Kojima, *Prog. Theor. Phys. Suppl.* **90**, 1 (1987); The latest version of our formulation is described in [36].
- [41] M. Shibata and K. Uryū, *Phys. Rev. D* **61**, 064001 (2000); *Prog. Theor. Phys.* **107**, 265 (2002).
- [42] M. Alcubierre, S. Brandt, B. Brügmann, D. Holz, E. Seidel, R. Takahashi, and J. Thornburg, *Int. J. Mod. Phys. D* **10**, 273 (2001).

- [43] M. Shibata, *Prog. Theor. Phys.* **104**, 325 (2000).
- [44] M. Shibata and Y. Sekiguchi, *Phys. Rev. D* **68**, 104020 (2003).
- [45] M. Shibata, *Prog. Theor. Phys.* **101**, 1199 (1999).
- [46] V. Moncrief, *Ann. of Phys.* **88**, 323 (1974).
- [47] M. Shibata, *Astrophys. J.* **595**, 992 (2003).
- [48] S. L. Shapiro and S. A. Teukolsky, *Black Holes, White Dwarfs, and Neutron Stars* (Wiley Interscience, New York, 1983).
- [49] H. A. Bethe, *Rev. Mod. Phys.* **62**, 801 (1990).
- [50] E.g., H. Komatsu, Y. Eriguchi, and I. Hachisu, *Mon. Not. R. Astron. Soc.*, **237**, 355 (1989); **239**, 153 (1989).
- [51] N. Stergioulas, *Living Rev. Relativ.* **6**, 3 (2003), <http://www.livingreviews.org/lrr-2003-3>.
- [52] Y. Sekiguchi and M. Shibata, in preparation.
- [53] M. Shibata and S. L. Shapiro, *Astrophys. J. Lett.* **572**, L39 (2002).
- [54] J. W. York, Jr., in *Sources of Gravitational Radiation*, ed. L. L. Smarr (Cambridge University Press, 1979), p. 83.
- [55] J. M. Centrella, K. C. B. New, L. Lowe, and J. D. Brown, *Astrophys. J. Lett.* **550**, 193 (2001).
- [56] M. Saijo, T. W. Baumgarte, and S. L. Shapiro, *Astrophys. J.* **595**, 352 (2003).
- [57] S. E. Woosley, *Astrophys. J.* **405**, 273 (1993); B. Paczynski, *Astrophys. J. Lett.* **494**, L45 (1998); A. I. MacFadyen and S. E. Woosley, *Astrophys. J.* **524**, 262 (1999); A. I. MacFadyen, S. E. Woosley, and A. Heger, *Astrophys. J.* **550**, 410 (2001).
- [58] T. Piran, *Phys. Rep.* **314**, 575 (1999); *ibid.* **333**, 529 (2000).
- [59] T. W. Baumgarte, S. L. Shapiro, and M. Shibata, *Astrophys. J.* **528**, L29 (2000).
- [60] C. L. Fryer, S. E. Woosley, and A. Heger, *Astrophys. J.* **550**, 372 (2001).
- [61] J. R. Bond, W. D. Arnett, and B. J. Carr, *Astrophys. J.* **280**, 825 (1984).
- [62] M. Shibata, *Astrophys. J.* **605**, 350 (2004).
- [63] S. M. Miyama, C. Hayashi, and S. Narita, *Astrophys. J.* **279**, 621 (1984); S. M. Miyama, *Pub. Astron. Soc. Japan* **44**, 193 (1992).
- [64] K. D. Kokkotas, in *Relativistic Gravitation and Gravitational Radiation*, edited by J.-P. Lasota and J.-A. Marck (Cambridge University Press, Cambridge, England, 1997), p. 89.
- [65] D. Lai and S. L. Shapiro, *Astrophys. J.* **442**, 259 (1995).
- [66] M. Shibata and S. Karino, *Phys. Rev. D* **70**, 084024 (2004).
- [67] S. Ou, J. E. Tohline, and L. Lindblom, [astro-ph/0406037](http://arxiv.org/abs/astro-ph/0406037).
- [68] J. M. Lattimer and F. D. Swesty, *Nucl. Phys. A* **535**, 331 (1991).
- [69] H. Shen, H. Toki, K. Oyamatsu, and K. Sumiyoshi, *Nucl. Phys. A* **637**, 435 (1998); *Prog. Theor. Phys.* **100**, 1013 (1998).
- [70] A. Burrows and J. M. Lattimer, *Astrophys. J.* **307**, 178 (1987).